

NATIONAL UNIVERSITY OF HO CHI MINH CITY
UNIVERSITY OF SCIENCE
FACULTY OF PHYSICS - ENGINEERING PHYSICS

—oo—

UNDERGRADUATE THESIS

Thesis title:

Hofstadter butterfly in transition metal
dichalcogenide monolayers

Student: Tran Khoi Nguyen
Supervisor: Dr. Huynh Thanh Duc

Ho Chi Minh City, 2025

**NATIONAL UNIVERSITY OF HO CHI MINH CITY
UNIVERSITY OF SCIENCE
FACULTY OF PHYSICS - ENGINEERING PHYSICS**

UNDERGRADUATE THESIS

Thesis title:

**Hofstadter butterfly in transition metal
dichalcogenide monolayers**

Major code: 7440102

Specialization: Theoretical Physics

**Student: Tran Khoi Nguyen
Supervisor: Dr. Huynh Thanh Duc**

Ho Chi Minh City, 2025

GUARANTEE

I guarantee to independently conducting the calculation of the Hofstadter butterfly of an ideal two-dimensional system of MoS₂ for my bachelor thesis, under the supervision of Dr. Huynh Thanh Duc.

The contexts are included in this graduation thesis are totally accurate and honest.

STUDENT
(Signature)

Tran Khoi Nguyen

ACKNOWLEDGMENTS

This thesis would not have been possible without the help and support of a large number of individuals. Firstly, I would like to thank my family members, especially my beloved mother and my sister, who have totally encouraged me on my path of becoming a scientist and helped me tremendously in all ways possible. Without them, I would not have enough much confidence to finish this. Thank you.

I am deeply greeted to my supervisor Dr. Huynh Thanh Duc from the Institute of Physics, Ho Chi Minh city, who taught me not only knowledges, gave me advise but also wholeheartedly encouraged and guided me every steps of the way. I would like to thank Master Le Minh Chau from the Institute of Physics and Vo Chau Duc Phuong from ICTP, who helped me at the very first step of this thesis. I would also like to acknowledge with gratitude to Dr. Vu Quang Tuyen, Dr. Vo Quoc Phong and Dr. Nguyen Huu Nha from the Department of Theoretical Physics. They have trully inspired me on the way becoming a physicist.

Finally, I would like to thank my colleagues at the University of Science including Dao Duy Tung, Le Quoc Duy, Ho Ngo Thanh Khoa, Pham Hoang Minh Quang, Truong Anh Duy, Pham Nguyen Thanh Dat.

Ho Chi Minh city, July, 2025

Tran Khoi Nguyen

TABLE OF CONTENTS

1	INTRODUCTION	1
2	THEORY	3
2.1	Three-band tight binding method without magnetic field	3
2.2	Three-band tight binding method under a magnetic field	9
2.3	Landau levels	19
2.4	Hall effects	22
2.4.1	The classical Hall effect	22
2.4.2	The Quantum Hall effect	23
2.4.3	Color the Hofstadter butterfly	25
3	SUMMARY	30
3.1	Conclusions	30
3.2	Discussions and Future work	31
A	Matrix elements of the TB Hamiltonian without SOC	32
B	Details of the Peierls substitution	38
C	Solving the Diophantine equation	39
REFERENCES		40

LIST OF FIGURES

2.1	TMD structure and its first Brillouin zone.	3
2.2	The hexagonal structure with neighbor hoppings.	5
2.3	Band structure of MoS ₂ material along Γ -K direction	8
2.4	TMD with six neighbors atom M rewrite with the site index.	11
2.5	Magnetic unit cell for TMD monolayers.	13
2.6	A visualization of super matrix.	15
2.7	Hofstadter butterfly for TMD.	16
2.8	Banstructure with SOC.	18
2.9	Banstructure with SOC.	19
2.10	Landau levels in Hofstadter butterfly.	21
2.11	Logitudinal resistance and Hall resistance plot.	23
2.12	Quantum Hall effect by von Klitzing.	24
2.13	Colored points version of Hofstadter butterfly.	27
2.14	Gaps color-coded Hofstadter butterfly for NN case.	28
2.15	Gaps color-coded Hofstadter butterfly for TNN case.	29
A.1	Showcase NN Hofstadter's butterflies of MX ₂ monolayers.	35
A.2	Showcase TNN Hofstadter's butterflies of MX ₂ monolayers.	37

LIST OF TABLES

2.1	Coordinates relative of hopping terms.	6
2.2	Symmetry operators of the D3h point group.	7
A.1	Fitted parameters NN.	34
A.2	Fitted parameters TNN.	36
C.1	Values of Chern numbers.	39

LIST OF ABBREVIATIONS

TMD transition metal dichalcogenides	1
TB tight-binding	5
TBM tight-binding model	viii
NN nearest-neighbor	4
NNN next nearest-neighbor	5
TNN third-nearest-neighbor	5
2D two-dimensional	1
BZ Brillouin zone	8
GGA generalized-gradient approximation	16
LDA local-density approximation	16
SOC spin orbit coupling	17
LLs Landau levels	17
IQHE integer Quantum Hall effect	23

FQHE fractional Quantum Hall effect	23
TKNN Thouless-Kohmoto-Nightingale-Nijs	25
DOS Density of state	27
VB valence band	31
CB conduction band	31

Abstract

Hofstadter's butterfly has been studied experimentally for 50 years. It was first discovered by computer scientist Douglas Hofstadter. This thesis explores the electronic phenomena in material systems, particularly focusing on monolayer transition metal dichalcogenides. A key focus is on understanding Hofstadter physics. We begin by studying a minimal three-band tight-binding model (TBM) in order to describe the electronic structure of TMD monolayer. We, then, analyze the resulting Hofstadter spectrum under an external magnetic field, revealing the rich fractal structure. Building on this framework, we further explore related quantum phenomena including Landau levels and quantum Hall effect.

Keywords: Tight-binding model, Hofstadter butterfly, Honeycomb lattice, Landau levels, quantum Hall effect, transition metal dichalcogenides.

CHAPTER 1

INTRODUCTION

Since the isolation of graphene in 2004, research on the field of two-dimensional (2D) materials has noticeably grown into a major branch of physical science with a wide range of applications. Their unique 2D structure offers an open canvas to tailor and functionalize through layer number, defects, morphology, moiré patterns, strain, and other tunable properties. 2D materials, such as graphene and transition metal dichalcogenides (TMD), have become a focal point in condensed matter physics due to their extraordinary electronic properties. Over the years, researchers have focused on graphene, with hope that its potential to replace silicon, enabling the continuation of Moore's law in next-generation semiconductor devices. However, in recent years, owing to their potentials, the number of scholarly papers researching graphene's use was enormous, reached a peak of thousand publications annually in 2021. Meanwhile, TMD have created tremendous interest among materials scientists, on account of their huge potential for new types of electronics, optoelectronics and superconductivity. Atomically thin 2D TMD have led to a variety of promising technologies for nanoelectronic, sensing and optoelectronics. Unlike graphene, many 2D TMD are naturally semiconductors and enormously posses potential to be made into ultra-small and low power transistors than silicon. These materials consist of large atom from the transistion metal elements that lies in the middle of the periodic table are sandwiched by two layers of atoms from the chalcogenide elements, such as sulfur or selenium, forming a three-layer sandwich called a transistion metal dichalcogenides.

Another majority opportunity is unraveling the fundamental behind the unique properties of 2D materials. These systems exhibit a various interesting quantum effects, such as superconductivity, weak localization, tological insulation, and others. In some cases, these quantum effects can lead to novel applications, such as valleytronics or twistronics.

The Hofstadter butterfly have been studied for nearly 50 years with various ranging reportedly from 2D symmetry lattice such as square lattice, triangular lattice, honeycomb

lattice, Kagome lattice to Lieb’s lattice, Mielke’s lattice, Tasaki’s lattice under an uniform magnetic field. The first Hofstadter butterfly was originally made for an electron moving in a 2D square lattice by computer scientist Douglas Hofstadter. The behaviour of an electron in such a quantum system could produce an energy spectrum which leads to a self-similar recursive Landau level spectrum resembling butterfly wings. The idea behind Hofstadter’s butterfly is that you’re looking at how the band structure of electrons moves when you have the magnetic field on one axis and the electrons’ energies on the other, and plotted on that diagram, the band forms a fractal structure that looks like a butterfly.

This thesis is mainly organized to explore the electronic structure in 2D material systems with external magnetic fields, with a particular focus on monolayer TMD. Beginning with Section 2.1, where we introduce the tight-binding theory with some important approximations such as independent electron approximation, tightly bound electron approximation, parabola approximation. After that, based on the minimal model introduced in Ref. [2] we derived the parameters for the tight-binding model. The parameters in the model was chosen to fit the band structure obtained from *ab initio* calculation. In Section 2.2, we first meets the Hofstadter butterfly of monolayer TMD by deriving the Hamiltonian in the tight-binding model under a fractional magnetic field and analyzing the result Hofstadter spectrum. Delving into the Hofstadter physics, we begin exploring the butterfly with quantum phenomena such as Landau levels and quantum Hall effects. These are discussed in Section. 2.2 and Section 2.3. The results obtained exhibits an interesting phenomena. Ultimately, chapter 3 concludes the thesis by summarizing the focus key finding and highlighting the potential avenues for future research. This includes the exploration of interaction effects beyond tight-binding theory and the extension of material physics studies to other tunable properties, such as Moiré systems or twisted bilayer systems to 2D materials.

CHAPTER 2

THEORY

2.1 Three-band tight binding method without magnetic field

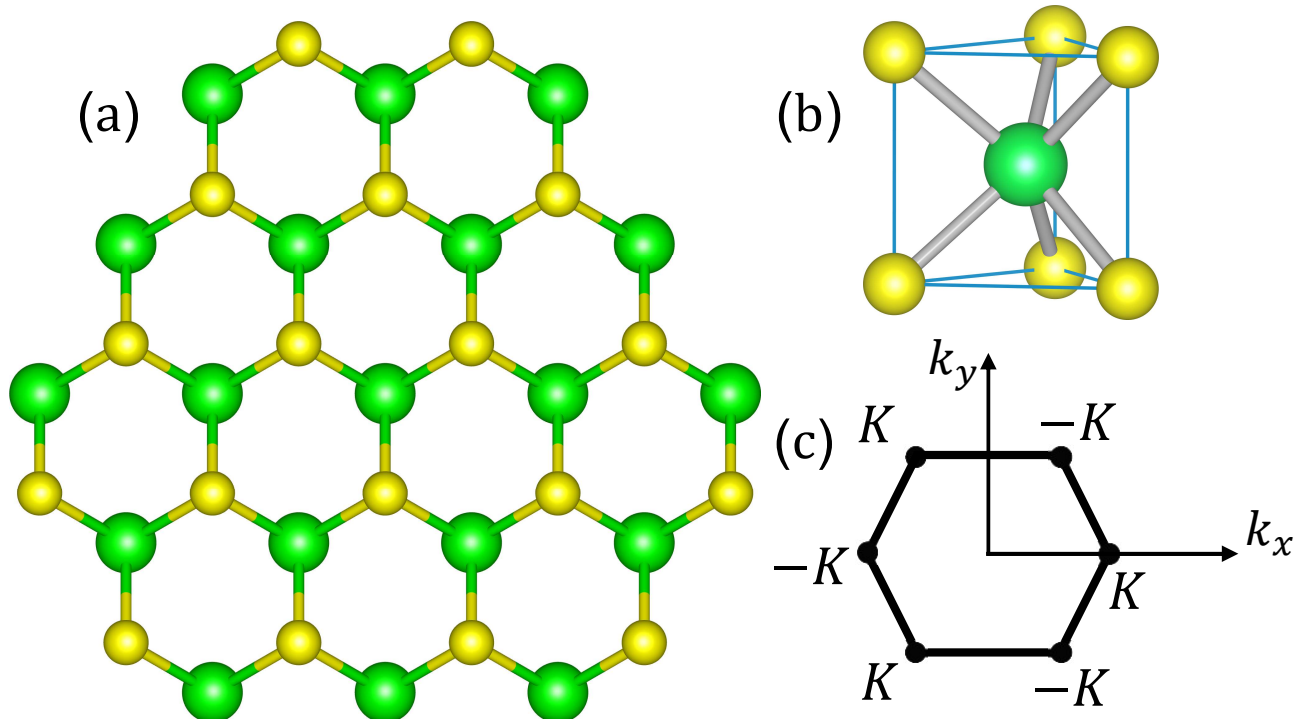


Figure 2.1: (a) Top view of monolayer MX_2 . The large sphere is M atom and the small sphere is X.

The time-independent Schrödinger equation for an electron in the crystal has the form

$$\left[-\frac{\hbar^2 \nabla^2}{2m} + U_0(\mathbf{r}) \right] \psi_{\lambda, \mathbf{k}}(\mathbf{r}) = \varepsilon_{\lambda}(\mathbf{k}) \psi_{\lambda, \mathbf{k}}(\mathbf{r}), \quad (2.1)$$

where $U_0(\mathbf{r})$ is the periodic lattice potential, $\psi_{\lambda,\mathbf{k}}(\mathbf{r})$ is the Bloch wavefunction of an electron in band λ with wave vector \mathbf{k} and $\varepsilon_{\lambda}(\mathbf{k})$ is the band structure.

In the tight-binding model (TBM), the single-electron Bloch wavefunction can be expressed in terms of atomic orbitals as follows

$$\psi_{\lambda,\mathbf{k}}(\mathbf{r}) = \sum_{j,i} C_{ji}^{\lambda}(\mathbf{k}) \sum_{\mathbf{R}} e^{i\mathbf{k}\cdot(\mathbf{R}+\mathbf{r}_i)} \phi_j(\mathbf{r} - \mathbf{R} - \mathbf{r}_i), \quad (2.2)$$

where $\phi_j(\mathbf{r} - \mathbf{R} - \mathbf{r}_i)$ is the orbital j of an atom i localized on a lattice site \mathbf{R} , in which \mathbf{r}_i is the relative position of the atom i in the unit cell, and $C_{ji}^{\lambda}(\mathbf{k})$ are the coefficients of linear expansion.

The unit cell of TMD involve one transition metal atom M and two chalcogenide atoms X. From the *ab initio* calculations, it is shown that the electron states near the band edges of MX_2 are mainly contributed from the three d orbital of M atom, namely $d_{z^2}, d_{xy}, d_{x^2-y^2}$ [2]. Since only the orbitals of atom M is included, we ignore the sum over the atom \mathbf{r}_i in the unit cell in Eq. (2.2). This model is called the three-band tight binding model. The three orbitals's wave function of M atom are denoted as

$$|\phi_1\rangle = |d_{z^2}\rangle; \quad |\phi_2\rangle = |d_{xy}\rangle; \quad |\phi_3\rangle = |d_{x^2-y^2}\rangle. \quad (2.3)$$

The Bloch wavefunction in this model has the form

$$\psi_{\lambda,\mathbf{k}}(\mathbf{r}) = \sum_{j=1}^3 C_j^{\lambda}(\mathbf{k}) \sum_{\mathbf{R}} e^{i\mathbf{k}\cdot\mathbf{R}} \phi_j(\mathbf{r} - \mathbf{R}). \quad (2.4)$$

The coefficients $C_j^{\lambda}(\mathbf{k})$ are the solutions of the eigenvalue equation

$$\sum_{jj'}^3 \left[H_{jj'}^{\text{TB}}(\mathbf{k}) - \varepsilon_{\lambda}(\mathbf{k}) S_{jj'}(\mathbf{k}) \right] C_j^{\lambda}(\mathbf{k}) = 0, \quad (2.5)$$

where

$$H_{jj'}^{\text{TB}}(\mathbf{k}) = \sum_{\mathbf{R}} e^{i\mathbf{k}\cdot\mathbf{R}} \langle \phi_j(\mathbf{r}) | \left[-\frac{\hbar^2 \nabla^2}{2m} + U_0(\mathbf{r}) \right] | \phi_{j'}(\mathbf{r} - \mathbf{R}) \rangle, \quad (2.6)$$

and

$$S_{jj'}(\mathbf{k}) = \sum_{\mathbf{R}} \langle \phi_j(\mathbf{r}) | \phi_{j'}(\mathbf{r} - \mathbf{R}) \rangle \approx \delta_{jj'}. \quad (2.7)$$

The three-band tight-binding model often called the nearest-neighbor (NN) since it only includes nearest-neighbor hopping does a decent job matching *ab initio* results near the band edges. However, it starts to break down in other parts of the band structure.

This is because the model completely ignores the p orbitals from the X atoms, which still contributions to the conduction bands at Γ and the valence bands at M. The matrix elements of the tight-binding (TB) Hamiltonian Eq. (2.6) are

$$\begin{aligned}
H_{jj'}^{\text{TNN}}(\mathbf{k}) = & \mathcal{E}_{jj'}(\mathbf{0}) + e^{i\mathbf{k}\cdot\mathbf{R}_1} \mathcal{E}_{jj'}(\mathbf{R}_1) + e^{i\mathbf{k}\cdot\mathbf{R}_2} \mathcal{E}_{jj'}(\mathbf{R}_2) + e^{i\mathbf{k}\cdot\mathbf{R}_3} \mathcal{E}_{jj'}(\mathbf{R}_3) \\
& + e^{i\mathbf{k}\cdot\mathbf{R}_4} \mathcal{E}_{jj'}(\mathbf{R}_4) + e^{i\mathbf{k}\cdot\mathbf{R}_5} \mathcal{E}_{jj'}(\mathbf{R}_5) + e^{i\mathbf{k}\cdot\mathbf{R}_6} \mathcal{E}_{jj'}(\mathbf{R}_6) \\
& + e^{i\mathbf{k}\cdot\tilde{\mathbf{R}}_1} \mathcal{E}_{jj'}(\tilde{\mathbf{R}}_1) + e^{i\mathbf{k}\cdot\tilde{\mathbf{R}}_2} \mathcal{E}_{jj'}(\tilde{\mathbf{R}}_2) + e^{i\mathbf{k}\cdot\tilde{\mathbf{R}}_3} \mathcal{E}_{jj'}(\tilde{\mathbf{R}}_3) \\
& + e^{i\mathbf{k}\cdot\tilde{\mathbf{R}}_4} \mathcal{E}_{jj'}(\tilde{\mathbf{R}}_4) + e^{i\mathbf{k}\cdot\tilde{\mathbf{R}}_5} \mathcal{E}_{jj'}(\tilde{\mathbf{R}}_5) + e^{i\mathbf{k}\cdot\tilde{\mathbf{R}}_6} \mathcal{E}_{jj'}(\tilde{\mathbf{R}}_6) \\
& + e^{i\mathbf{k}\cdot 2\mathbf{R}_1} \mathcal{E}_{jj'}(2\mathbf{R}_1) + e^{i\mathbf{k}\cdot 2\mathbf{R}_2} \mathcal{E}_{jj'}(2\mathbf{R}_2) + e^{i\mathbf{k}\cdot 2\mathbf{R}_3} \mathcal{E}_{jj'}(2\mathbf{R}_3) \\
& + e^{i\mathbf{k}\cdot 2\mathbf{R}_4} \mathcal{E}_{jj'}(2\mathbf{R}_4) + e^{i\mathbf{k}\cdot 2\mathbf{R}_5} \mathcal{E}_{jj'}(2\mathbf{R}_5) + e^{i\mathbf{k}\cdot 2\mathbf{R}_6} \mathcal{E}_{jj'}(2\mathbf{R}_6)
\end{aligned} \tag{2.8}$$

where

$$\mathcal{E}_{jj'}(\mathbf{R}) = \langle \phi_j(\mathbf{r}) | \left[-\frac{\hbar^2 \nabla^2}{2m} + U_0(\mathbf{r}) \right] | \phi_{j'}(\mathbf{r} - \mathbf{R}) \rangle, \tag{2.9}$$

and \mathbf{R}_i , $\tilde{\mathbf{R}}_i$ and $2\mathbf{R}_i$ are one of the NN, next nearest-neighbor (NNN) and third-nearest-neighbor (TNN) vectors, respectively, where $i = 1, \dots, 6$, see in Fig (2.2). Table (2.1) summarizes the coordinates of hopping vectors considered in the model.

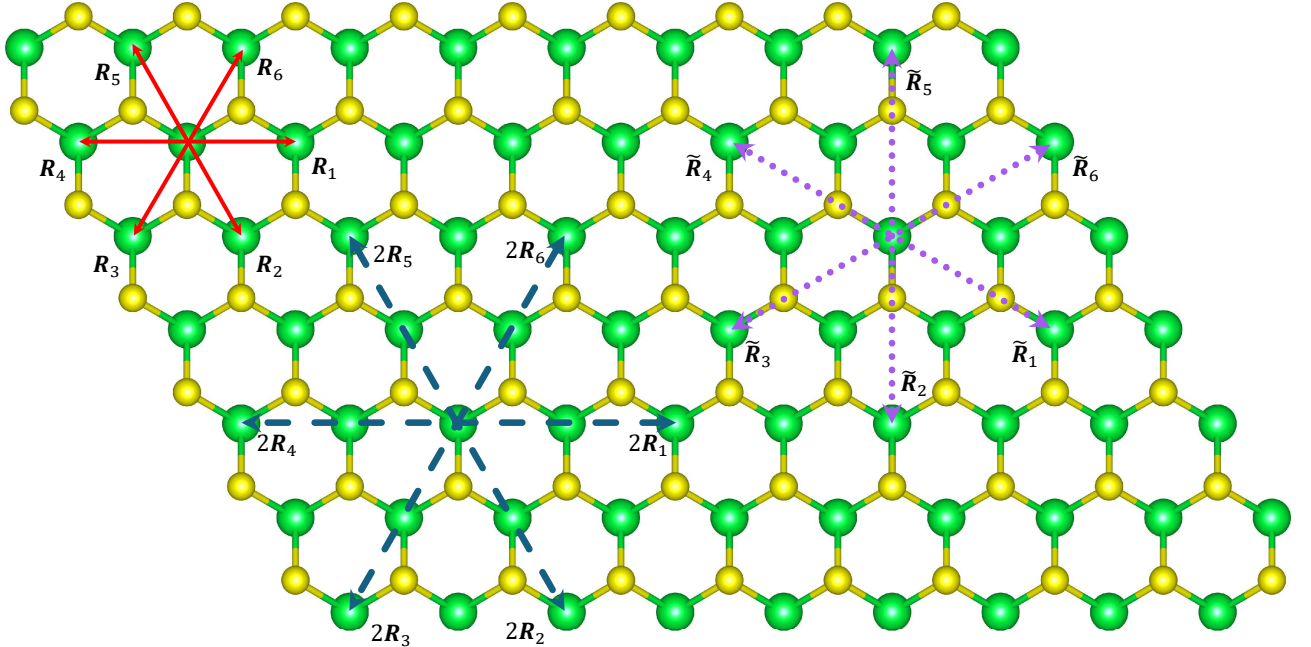


Figure 2.2: The hexagonal structure of the TMD with the metal atoms at the green larger circles and the chalcogen atoms at the smaller yellow circles. The solid red, dash blue and dot purple arrows represent the NN (\mathbf{R}_i), NNN ($\tilde{\mathbf{R}}_i$) and TNN ($2\mathbf{R}_i$), respectively, where $i = 1, \dots, 6$.

Vector	Hopping relative coordinates	Cartesian's coordinates
\mathbf{R}_1	$(m, n) \rightarrow (m + 2, n)$	$a(1, 0, 0)$
\mathbf{R}_2	$(m, n) \rightarrow (m + 1, n - 1)$	$a\left(\frac{1}{2}, -\frac{\sqrt{3}}{2}, 0\right)$
\mathbf{R}_3	$(m, n) \rightarrow (m - 1, n - 1)$	$a\left(-\frac{1}{2}, -\frac{\sqrt{3}}{2}, 0\right)$
\mathbf{R}_4	$(m, n) \rightarrow (m - 2, n)$	$a(-1, 0, 0)$
\mathbf{R}_5	$(m, n) \rightarrow (m - 1, n + 1)$	$a\left(-\frac{1}{2}, \frac{\sqrt{3}}{2}, 0\right)$
\mathbf{R}_6	$(m, n) \rightarrow (m + 1, n + 1)$	$a\left(-\frac{1}{2}, \frac{\sqrt{3}}{2}, 0\right)$
$\tilde{\mathbf{R}}_1$	$(m, n) \rightarrow (m + 3, n - 1)$	$l\left(\frac{\sqrt{3}}{2}, -\frac{1}{2}, 0\right)$
$\tilde{\mathbf{R}}_2$	$(m, n) \rightarrow (m, n - 2)$	$l(0, -1, 0)$
$\tilde{\mathbf{R}}_3$	$(m, n) \rightarrow (m - 3, n - 1)$	$l\left(-\frac{\sqrt{3}}{2}, -\frac{1}{2}, 0\right)$
$\tilde{\mathbf{R}}_4$	$(m, n) \rightarrow (m - 3, n + 1)$	$l\left(-\frac{\sqrt{3}}{2}, \frac{1}{2}, 0\right)$
$\tilde{\mathbf{R}}_5$	$(m, n) \rightarrow (m, n + 2)$	$l(0, -1, 0)$
$\tilde{\mathbf{R}}_6$	$(m, n) \rightarrow (m + 3, n + 1)$	$l\left(\frac{\sqrt{3}}{2}, \frac{1}{2}, 0\right)$
$2\mathbf{R}_1$	$(m, n) \rightarrow (m + 4, n)$	$a(2, 0, 0)$
$2\mathbf{R}_2$	$(m, n) \rightarrow (m + 2, n - 2)$	$a(1, -\sqrt{3}, 0)$
$2\mathbf{R}_3$	$(m, n) \rightarrow (m - 2, n - 2)$	$a(-1, -\sqrt{3}, 0)$
$2\mathbf{R}_4$	$(m, n) \rightarrow (m - 4, n)$	$a(-2, 0, 0)$
$2\mathbf{R}_5$	$(m, n) \rightarrow (m - 2, n + 2)$	$a(-1, \sqrt{3}, 0)$
$2\mathbf{R}_6$	$(m, n) \rightarrow (m + 2, n + 2)$	$a(1, \sqrt{3}, 0)$

Table 2.1: Hopping vectors used in the model and their hopping respective relative coordinates to the original site (m, n) , where $a = 3.190\text{\AA}$ is lattice constant and $l = a\sqrt{3}$.

One parameterizes the matrices $\mathcal{E}(\mathbf{0}), \mathcal{E}(\mathbf{R}_1), \mathcal{E}(\tilde{\mathbf{R}}_1), \mathcal{E}(\tilde{\mathbf{R}}_4)$ and $\mathcal{E}(2\mathbf{R}_1)$ by

$$\begin{aligned} \mathcal{E}(\mathbf{0}) &= \begin{pmatrix} \epsilon_1 & 0 & 0 \\ 0 & \epsilon_2 & 0 \\ 0 & 0 & \epsilon_2 \end{pmatrix}, \mathcal{E}(\mathbf{R}_1) = \begin{pmatrix} t_0 & t_1 & t_2 \\ -t_1 & t_{11} & t_{12} \\ t_2 & -t_{12} & t_{22} \end{pmatrix}, \mathcal{E}(2\mathbf{R}_1) = \begin{pmatrix} u_0 & u_1 & u_2 \\ -u_1 & u_{11} & u_{12} \\ u_2 & -u_{12} & u_{22} \end{pmatrix}, \\ \mathcal{E}(\tilde{\mathbf{R}}_1) &= \begin{pmatrix} r_0 & r_1 & -\frac{r_1}{\sqrt{3}} \\ r_2 & r_{11} & r_{12} \\ -\frac{r_2}{\sqrt{3}} & r_{12} & r_{11} + \frac{2\sqrt{3}}{3}r_{12} \end{pmatrix}, \mathcal{E}(\tilde{\mathbf{R}}_4) = \mathcal{E}(\tilde{\mathbf{R}}_1)^T = \begin{pmatrix} r_0 & r_2 & -\frac{r_2}{\sqrt{3}} \\ r_1 & r_{11} & r_{12} \\ -\frac{r_1}{\sqrt{3}} & r_{12} & r_{11} + \frac{2\sqrt{3}}{3}r_{12} \end{pmatrix}. \end{aligned} \quad (2.10)$$

Given $\mathcal{E}(\mathbf{R}_1), \mathcal{E}(2\mathbf{R}_1), \mathcal{E}(\tilde{\mathbf{R}}_1), \mathcal{E}(\tilde{\mathbf{R}}_4)$, the matrix $\mathcal{E}(\mathbf{R}_i)$ corresponding to all neighbor sites \mathbf{R}_i can be generated by

$$\mathcal{E}(g_n \mathbf{R}) = D(g_n) \mathcal{E}(\mathbf{R}) D^\dagger(g_n), \quad (2.11)$$

g_n	x'	y'	z'	z'^2	$x'y'$	$\frac{1}{2}(x'^2 - y'^2)$
E	x	y	z	z^2	xy	$\frac{1}{2}(x^2 - y^2)$
$C_3(-\frac{2\pi}{3})$	$-\frac{1}{2}x + \frac{\sqrt{3}}{2}y$	$-\frac{\sqrt{3}}{2}x - \frac{1}{2}y$	z	z^2	$-\frac{1}{2}xy + \frac{\sqrt{3}}{4}(x^2 + y^2)$	$-\frac{\sqrt{3}}{2}xy - \frac{1}{4}(x^2 - y^2)$
$C_3(-\frac{4\pi}{3})$	$-\frac{1}{2}x - \frac{\sqrt{3}}{2}y$	$\frac{\sqrt{3}}{2}x + \frac{1}{2}y$	z	z^2	$-\frac{1}{2}xy - \frac{\sqrt{3}}{4}(x^2 + y^2)$	$\frac{\sqrt{3}}{2}xy - \frac{1}{4}(x^2 - y^2)$
$C_2(-\pi)$	$-x$	$-y$	z	z^2	xy	$\frac{1}{2}(x^2 - y^2)$
σ_ν	$-x$	y	z	z^2	$-xy$	$\frac{1}{2}(x^2 - y^2)$
σ'_ν	$\frac{1}{2}x - \frac{\sqrt{3}}{2}$	$-\frac{\sqrt{3}}{2}x - \frac{1}{2}y$	z	z^2	$\frac{1}{2}xy - \frac{\sqrt{3}}{4}(x^2 + y^2)$	$-\frac{\sqrt{3}}{2}xy - \frac{1}{4}(x^2 - y^2)$
σ''_ν	$\frac{1}{2}x + \frac{\sqrt{3}}{2}$	$\frac{\sqrt{3}}{2}x - \frac{1}{2}y$	z	z^2	$\frac{1}{2}xy + \frac{\sqrt{3}}{4}(x^2 + y^2)$	$\frac{\sqrt{3}}{2}xy - \frac{1}{4}(x^2 - y^2)$

Table 2.2: Some symmetry operators of the D_{3h} point group on basis functions taking (x, y, z) into (x', y', z') . $C_3(-\frac{2\pi}{3})$ and $C_3(-\frac{4\pi}{3})$ are the rotations by $\frac{-2\pi}{3}$ and $\frac{-4\pi}{3}$ around the z axis, respectively. σ_ν is the reflection angular bisector of R_1 and R_6 in Fig. 2.1, and $\sigma'_\nu, \sigma''_\nu$ are obtained through rotating σ_ν around the z axis by $2\pi/3$ and $4\pi/3$, respectively.

where $D(g_n)$ is the matrix of the irreducible representation, g_n are symmetry operators of D_{3h} point groups, $\{E, 2C_3, 3C_2, 2S_3, \sigma_h, 3\sigma_\nu\}$, see in Appendix A for more details about the calculation. Table 2.2 depicts the transformation of the basis functions under the action of symmetry operators. Also, from Table 2.2, we obtain irreducible matrices as follows

$$\begin{aligned}
D(C_3(-\frac{2\pi}{3})) &= \begin{pmatrix} 1 & 0 & 0 \\ 0 & -1/2 & \sqrt{3}/2 \\ 0 & -\sqrt{3}/2 & -1/2 \end{pmatrix}, & D(C_3(-\frac{4\pi}{3})) &= \begin{pmatrix} 1 & 0 & 0 \\ 0 & -1/2 & -\sqrt{3}/2 \\ 0 & \sqrt{3}/2 & -1/2 \end{pmatrix}, \\
D(\sigma_\nu) &= \begin{pmatrix} 1 & 0 & 0 \\ 0 & -1 & 0 \\ 0 & 0 & 1 \end{pmatrix}, & D(\sigma'_\nu) &= \begin{pmatrix} 1 & 0 & 0 \\ 0 & 1/2 & -\sqrt{3}/2 \\ 0 & -\sqrt{3}/2 & -1/2 \end{pmatrix}, \\
D(\sigma''_\nu) &= \begin{pmatrix} 1 & 0 & 0 \\ 0 & 1/2 & \sqrt{3}/2 \\ 0 & \sqrt{3}/2 & -1/2 \end{pmatrix}.
\end{aligned} \tag{2.12}$$

The remaining hopping matrices can be obtained by applying the C_3 rotation, mirror, and relation $\mathcal{E}(-\mathbf{R}) = \mathcal{E}(\mathbf{R})^T$. Therefore, we have the hopping terms for three-band TBM including TNN are given in Appendix A.

The TNN tight-binding Hamiltonian now can be written as

$$H^{\text{TNN}}(\mathbf{k}) = \begin{pmatrix} V_0 & V_1 & V_2 \\ V_1^* & V_{11} & V_{12} \\ V_2^* & V_{12}^* & V_{22} \end{pmatrix}, \tag{2.13}$$

where

$$\begin{aligned}
V_0 &= \epsilon_1 + 2t_0(2 \cos \alpha \cos \beta + \cos 2\alpha) + 2r_0(2 \cos 3\alpha \cos \beta + \cos 2\beta), \\
\text{Re}[V_1] &= -2\sqrt{3}t_2 \sin \alpha \sin \beta + 2(r_1 + r_2) \sin 3\alpha \sin \beta - 2\sqrt{3}u_2 \sin 2\alpha \sin 2\beta, \\
\text{Im}[V_1] &= 2t_1 \sin \alpha(2 \cos \alpha + \cos \beta) + 2(r_1 - r_2) \sin 3\alpha \cos \beta + 2u_1 \sin 2\alpha(2 \cos 2\alpha + \cos 2\beta) \\
\text{Re}[V_2] &= 2t_2(\cos 2\alpha - \cos \alpha \cos \beta) - \frac{2}{\sqrt{3}}(r_1 + r_2)(\cos 3\alpha \cos \beta - \cos 2\beta) \\
&\quad + 2u_2(\cos 4\alpha - \cos 2\alpha \cos 2\beta), \\
\text{Im}[V_2] &= 2\sqrt{3}t_1 \cos \alpha \sin \beta + \frac{2}{\sqrt{3}} \sin \beta(r_1 - r_2)(\cos 3\alpha + 2 \cos \beta), \\
V_{11} &= \epsilon_2 + (t_{11} + 3t_{22}) \cos \alpha \cos \beta + 2t_{11} \cos 2\alpha + 4r_{11} \cos 3\alpha \cos \beta \\
&\quad + 2(r_{11} + \sqrt{3}r_{12}) \cos 2\beta + (u_{11} + 3u_{22}) \cos 2\alpha \cos 2\beta + 2u_{11} \cos 4\alpha, \\
\text{Re}[V_{12}] &= \sqrt{3}(t_{22} - t_{11}) \sin \alpha \sin \beta + 4r_{12} \sin 3\alpha \sin \beta + \sqrt{3}(u_{22} - u_{11}) \sin 2\alpha \sin 2\beta, \\
\text{Im}[V_{12}] &= 4t_{12} \sin \alpha(\cos \alpha - \cos \beta) + 4u_{12} \sin 2\alpha(\cos 2\alpha - \cos 2\beta), \\
V_{22} &= \epsilon_2 + (3t_{11} + t_{22}) \cos \alpha \cos \beta + 2t_{22} \cos 2\alpha + 2r_{11}(2 \cos 3\alpha \cos \beta + \cos 2\beta) \\
&\quad + \frac{2}{\sqrt{3}}r_{12}(4 \cos 3\alpha \cos \beta - \cos 2\beta) + (3u_{11} + u_{22}) \cos 2\alpha \cos 2\beta + 2u_{22} \cos 4\alpha,
\end{aligned} \tag{2.14}$$

$$(\alpha, \beta) = \left(\frac{1}{2}k_x a, \frac{\sqrt{3}}{2}k_y a \right). \tag{2.15}$$

Nineteen additional parameters are depicted in Table A.2 are obtained by fitting the band with *ab initio* calculation results.

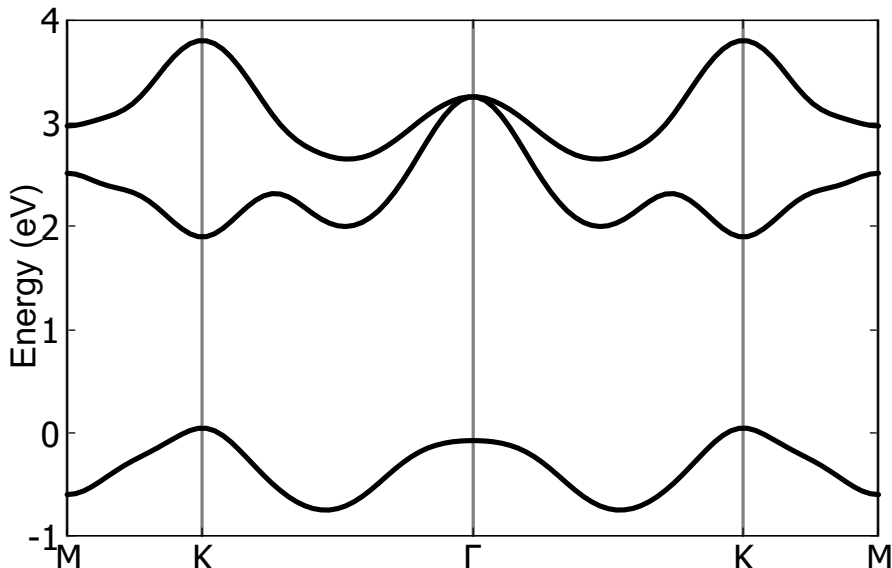


Figure 2.3: To obtain the band structure of monolayer MoS₂, the eigenvalue of the Hamiltonian needs to be found at each k point across the entire the Brillouin zone (BZ). This figure illustrates the band structure along Γ -K direction using (LDA) fitting parameters.

2.2 Three-band tight binding method under a magnetic field

Under an uniform magnetic field given by a vector potential $\mathbf{A}(\mathbf{r})$ the single electron Hamiltonian changes into

$$H = \frac{(-i\hbar\mathbf{\nabla} + e\mathbf{A}(\mathbf{r}))^2}{2m} + U_0(\mathbf{r}) + g^* \mu_B \mathbf{B} \cdot \mathbf{L}, \quad (2.16)$$

where $\mu_B = \frac{e\hbar}{2m}$ is Bohr magneton, g^* is an effective Landé g-factor, $\mathbf{B} = \mathbf{\nabla} \times \mathbf{A}$ is the uniform magnetic field, and \mathbf{L} is the angular momentum. It is possible to add a phase factor to the tight-binding wavefunction

$$\psi_{\lambda, \mathbf{k}}(\mathbf{r}) = \sum_{j=1}^3 C_j^\lambda(\mathbf{k}) \sum_{\mathbf{R}} e^{i\mathbf{k} \cdot \mathbf{R}} e^{\theta_{\mathbf{R}}(\mathbf{r})} \phi_j(\mathbf{r} - \mathbf{R}). \quad (2.17)$$

We now have

$$H_{jj'}(\mathbf{k}) = H_{jj'}^{\text{NN}}(\mathbf{k}) + H_{jj'}^Z(\mathbf{k}), \quad (2.18)$$

where

$$\begin{aligned} H_{jj'}^{\text{NN}}(\mathbf{k}) &= \sum_{\mathbf{R}} \langle \phi_j(\mathbf{r}) | e^{-i\theta_0(\mathbf{r})} \left[\frac{(-i\hbar\mathbf{\nabla} + e\mathbf{A}(\mathbf{r}))^2}{2m} + U_0(\mathbf{r}) \right] e^{i\mathbf{k} \cdot \mathbf{R}} e^{\theta_{\mathbf{R}}(\mathbf{r})} | \phi_{j'}(\mathbf{r} - \mathbf{R}) \rangle \\ &= \sum_{\mathbf{R}} \langle \phi_j(\mathbf{r}) | e^{i(\mathbf{k} \cdot \mathbf{R} + \theta_{\mathbf{R}} - \theta_0)} \left[\frac{(-i\hbar\mathbf{\nabla} + e\mathbf{A} + \hbar\mathbf{\nabla}\theta_{\mathbf{R}})^2}{2m} + U_0(\mathbf{r}) \right] | \phi_{j'}(\mathbf{r} - \mathbf{R}) \rangle, \end{aligned} \quad (2.19)$$

and

$$H_{jj'}^Z(\mathbf{k}) = g^* \mu_B \mathbf{B} \cdot \sum_{\mathbf{R}} \langle \phi_j(\mathbf{r}) | e^{i(\mathbf{k} \cdot \mathbf{R} + \theta_{\mathbf{R}} - \theta_0)} \mathbf{L} | \phi_{j'}(\mathbf{r} - \mathbf{R}) \rangle. \quad (2.20)$$

By choosing $\theta_{\mathbf{R}} = -\frac{e}{\hbar} \int_{\mathbf{R}}^{\mathbf{r}} \mathbf{A}(\mathbf{r}') \cdot d\mathbf{r}'$ as Peierls substitution, the Hamiltonian in Eq. (2.19) now reads

$$\begin{aligned} H_{jj'}^{\text{NN}}(\mathbf{k}) &= \sum_{\mathbf{R}} \langle \phi_j(\mathbf{r}) | e^{i\mathbf{k} \cdot \mathbf{R} - \frac{ie}{\hbar} \int_{\mathbf{R}}^{\mathbf{r}} \mathbf{A}(\mathbf{r}') \cdot d\mathbf{r}' + \frac{ie}{\hbar} \int_{\mathbf{0}}^{\mathbf{r}} \mathbf{A}(\mathbf{r}') \cdot d\mathbf{r}'} \left[-\frac{\hbar^2 \mathbf{\nabla}^2}{2m} + U_0(\mathbf{r}) \right] | \phi_{j'}(\mathbf{r} - \mathbf{R}) \rangle \\ &= \sum_{\mathbf{R}} e^{i\mathbf{k} \cdot \mathbf{R}} e^{\frac{ie}{\hbar} \int_{\mathbf{0}}^{\mathbf{R}} \mathbf{A}(\mathbf{r}') \cdot d\mathbf{r}'} \langle \phi_j(\mathbf{r}) | e^{-\frac{ie}{\hbar} \Phi_{\mathbf{R}, \mathbf{r}, \mathbf{0}}} \left[-\frac{\hbar^2 \mathbf{\nabla}^2}{2m} + U_0(\mathbf{r}) \right] | \phi_{j'}(\mathbf{r} - \mathbf{R}) \rangle, \end{aligned} \quad (2.21)$$

where $\Phi_{\mathbf{R}, \mathbf{r}, \mathbf{0}} = \oint_{\mathbf{R}, \mathbf{r}, \mathbf{0}} \mathbf{A}(\mathbf{r}') \cdot d\mathbf{r}'$ is the closed loop line integral of \mathbf{A} along the triangle points $\mathbf{R}, \mathbf{r}, \mathbf{0}$, and $\int_0^{\mathbf{R}} \mathbf{A}(\mathbf{r}') \cdot d\mathbf{r}'$ is the path integral along the two points $\mathbf{R}, \mathbf{0}$. Besides that, we have used the fact that

$$\int_{\mathbf{R}}^{\mathbf{r}} \mathbf{A}(\mathbf{r}') \cdot d\mathbf{r}' + \int_{\mathbf{r}}^{\mathbf{0}} \mathbf{A}(\mathbf{r}') \cdot d\mathbf{r}' = \Phi_{\mathbf{R}, \mathbf{r}, \mathbf{0}} - \int_0^{\mathbf{R}} \mathbf{A}(\mathbf{r}') \cdot d\mathbf{r}'. \quad (2.22)$$

We can show that the flux term $\Phi_{\mathbf{R}, \mathbf{r}, \mathbf{0}}$ is negligibly small [3] by two observations. When \mathbf{r} is far away from the lattice points \mathbf{R} and $\mathbf{0}$, the flux is large but since the atomic orbitals are highly localized at these two lattice points, the value of the hopping term is very small and the whole hopping term goes to zero. While \mathbf{r} is at or near any of these lattice points, the triangle formed is small, and assuming small magnetic field, the flux term $\Phi_{\mathbf{R}, \mathbf{r}, \mathbf{0}}$ goes to zero, which giving us the Hamiltonian as

$$H_{jj'}^{\text{TNN}}(\mathbf{k}) = \sum_{\mathbf{R}} e^{i\mathbf{k} \cdot \mathbf{R}} e^{\frac{ie}{\hbar} \int_0^{\mathbf{R}} \mathbf{A}(\mathbf{r}') \cdot d\mathbf{r}'} \langle \phi_j(\mathbf{r}) | \left[-\frac{\hbar^2 \nabla^2}{2m} + U_0(\mathbf{r}) \right] | \phi_{j'}(\mathbf{r} - \mathbf{R}) \rangle, \quad (2.23)$$

$$H_{jj'}^Z(\mathbf{k}) = g^* \mu_B \mathbf{B} \cdot \sum_{\mathbf{R}} e^{i\mathbf{k} \cdot \mathbf{R}} e^{\frac{ie}{\hbar} \int_0^{\mathbf{R}} \mathbf{A}(\mathbf{r}') \cdot d\mathbf{r}'} \langle \phi_j(\mathbf{r}) | \mathbf{L} | \phi_{j'}(\mathbf{r} - \mathbf{R}) \rangle. \quad (2.24)$$

Considering only NN, NNN, TNN hopping, Eq (2.23) becomes

$$\begin{aligned} H_{jj'}^{\text{TNN}}(\mathbf{k}) &= \sum_{\mathbf{R}} e^{i\mathbf{k} \cdot \mathbf{R}} e^{\frac{e}{\hbar} \int_0^{\mathbf{R}} A(\mathbf{r}') d\mathbf{r}'} \mathcal{E}_{jj'}(\mathbf{R}) \\ &= \mathcal{E}_{jj'}(\mathbf{0}) + e^{i\mathbf{k} \cdot \mathbf{R}_1} e^{\frac{e}{\hbar} \int_0^{\mathbf{R}_1} A(\mathbf{r}') d\mathbf{r}'} \mathcal{E}_{jj'}(\mathbf{R}_1) + e^{i\mathbf{k} \cdot \mathbf{R}_2} e^{\frac{e}{\hbar} \int_0^{\mathbf{R}_2} A(\mathbf{r}') d\mathbf{r}'} \mathcal{E}_{jj'}(\mathbf{R}_2) \\ &\quad + e^{i\mathbf{k} \cdot \mathbf{R}_3} e^{\frac{e}{\hbar} \int_0^{\mathbf{R}_3} A(\mathbf{r}') d\mathbf{r}'} \mathcal{E}_{jj'}(\mathbf{R}_3) + e^{i\mathbf{k} \cdot \mathbf{R}_4} e^{\frac{e}{\hbar} \int_0^{\mathbf{R}_4} A(\mathbf{r}') d\mathbf{r}'} \mathcal{E}_{jj'}(\mathbf{R}_4) \\ &\quad + e^{i\mathbf{k} \cdot \mathbf{R}_5} e^{\frac{e}{\hbar} \int_0^{\mathbf{R}_5} A(\mathbf{r}') d\mathbf{r}'} \mathcal{E}_{jj'}(\mathbf{R}_5) + e^{i\mathbf{k} \cdot \mathbf{R}_6} e^{\frac{e}{\hbar} \int_0^{\mathbf{R}_6} A(\mathbf{r}') d\mathbf{r}'} \mathcal{E}_{jj'}(\mathbf{R}_6) \\ &\quad + e^{i\mathbf{k} \cdot \tilde{\mathbf{R}}_1} e^{\frac{e}{\hbar} \int_0^{\tilde{\mathbf{R}}_1} A(\mathbf{r}') d\mathbf{r}'} \mathcal{E}_{jj'}(\tilde{\mathbf{R}}_1) + e^{i\mathbf{k} \cdot \tilde{\mathbf{R}}_2} e^{\frac{e}{\hbar} \int_0^{\tilde{\mathbf{R}}_2} A(\mathbf{r}') d\mathbf{r}'} \mathcal{E}_{jj'}(\tilde{\mathbf{R}}_2) \\ &\quad + e^{i\mathbf{k} \cdot \tilde{\mathbf{R}}_3} e^{\frac{e}{\hbar} \int_0^{\tilde{\mathbf{R}}_3} A(\mathbf{r}') d\mathbf{r}'} \mathcal{E}_{jj'}(\tilde{\mathbf{R}}_3) + e^{i\mathbf{k} \cdot \tilde{\mathbf{R}}_4} e^{\frac{e}{\hbar} \int_0^{\tilde{\mathbf{R}}_4} A(\mathbf{r}') d\mathbf{r}'} \mathcal{E}_{jj'}(\tilde{\mathbf{R}}_4) \\ &\quad + e^{i\mathbf{k} \cdot \tilde{\mathbf{R}}_5} e^{\frac{e}{\hbar} \int_0^{\tilde{\mathbf{R}}_5} A(\mathbf{r}') d\mathbf{r}'} \mathcal{E}_{jj'}(\tilde{\mathbf{R}}_5) + e^{i\mathbf{k} \cdot \tilde{\mathbf{R}}_6} e^{\frac{e}{\hbar} \int_0^{\tilde{\mathbf{R}}_6} A(\mathbf{r}') d\mathbf{r}'} \mathcal{E}_{jj'}(\tilde{\mathbf{R}}_6) \\ &\quad + e^{i\mathbf{k} \cdot \mathbf{R}'_1} e^{\frac{e}{\hbar} \int_0^{\mathbf{R}'_1} A(\mathbf{r}') d\mathbf{r}'} \mathcal{E}_{jj'}(\mathbf{R}'_1) + e^{i\mathbf{k} \cdot \mathbf{R}'_2} e^{\frac{e}{\hbar} \int_0^{\mathbf{R}'_2} A(\mathbf{r}') d\mathbf{r}'} \mathcal{E}_{jj'}(\mathbf{R}'_2) \\ &\quad + e^{i\mathbf{k} \cdot \mathbf{R}'_3} e^{\frac{e}{\hbar} \int_0^{\mathbf{R}'_3} A(\mathbf{r}') d\mathbf{r}'} \mathcal{E}_{jj'}(\mathbf{R}'_3) + e^{i\mathbf{k} \cdot \mathbf{R}'_4} e^{\frac{e}{\hbar} \int_0^{\mathbf{R}'_4} A(\mathbf{r}') d\mathbf{r}'} \mathcal{E}_{jj'}(\mathbf{R}'_4) \\ &\quad + e^{i\mathbf{k} \cdot \mathbf{R}'_5} e^{\frac{e}{\hbar} \int_0^{\mathbf{R}'_5} A(\mathbf{r}') d\mathbf{r}'} \mathcal{E}_{jj'}(\mathbf{R}'_5) + e^{i\mathbf{k} \cdot \mathbf{R}'_6} e^{\frac{e}{\hbar} \int_0^{\mathbf{R}'_6} A(\mathbf{r}') d\mathbf{r}'} \mathcal{E}_{jj'}(\mathbf{R}'_6), \end{aligned} \quad (2.25)$$

where $\tilde{\mathbf{R}}_i$ is of the NN vectors and $\mathbf{R}'_i = 2\mathbf{R}_i$ is one of the TNN vectors.

In the presence of a perpendicular magnetic field $\mathbf{B}\hat{z}$ applied to the plane of TMD, we choose the vector potential in the Landau gauge as $\mathbf{A} = (0, Bx, 0)$. Suppose that

the atom metal M is located at position $\mathbf{R}_{m,n} = \left(m\frac{a}{2}, n\frac{a\sqrt{3}}{2}\right)$, where $m, n \in \mathbb{Z}$, let us define a shorthand notation for these extra terms

$$\begin{aligned}\theta_{m,n}^{m',n'} &= \frac{e}{\hbar} \int_{m,n}^{m',n'} \mathbf{A}(\mathbf{r}) \cdot d\mathbf{r} \\ &= \frac{eB}{2\hbar} (x_m + x_{m'})(y_{n'} - y_n),\end{aligned}\tag{2.26}$$

in which $x_m = \frac{ma}{2}(m = \pm 1, \pm 2)$ and $y_n = \frac{na\sqrt{3}}{2}(n = 0, \pm 1)$ are the TNN coordinates and a being the lattice constant, are shown in Fig. (2.4). Details of this calculation is given in Appendix B.

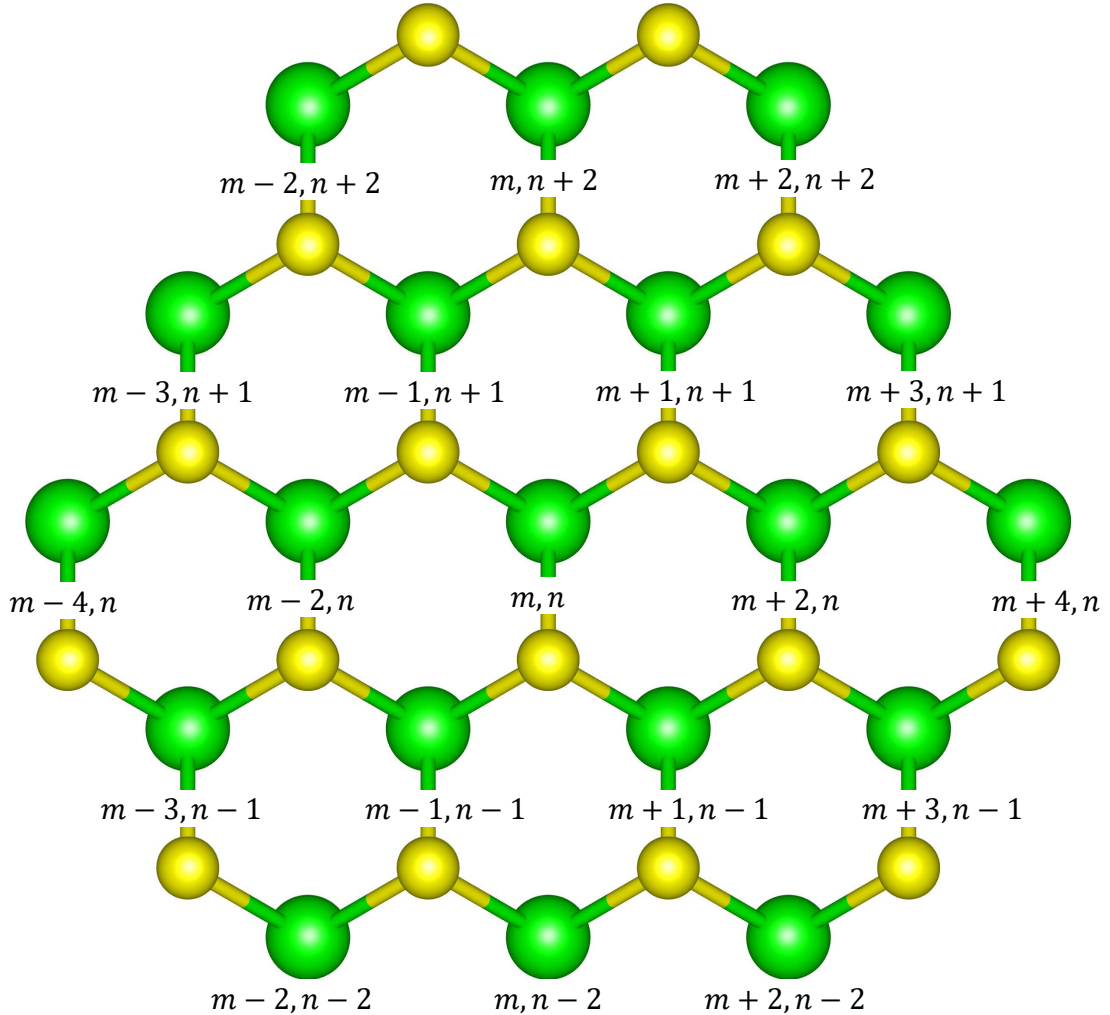


Figure 2.4: The TBM of TMD with eighteen neighbor atoms M rewrite with the site index.

Since $dy = 0$ along the x direction, $\theta_{m,n}^{m\pm 2,n} = 0$, and using TNN coordinates given for

lattice site in Table 2.1, the $\theta_{m,n}^{m',n'}$ can be written as

$$\theta_{m,n}^{m',n'} = \begin{cases} 0 & m' = m \pm 2, n' = n, \\ 0 & m' = m \pm 4, n' = n, \\ \pm \frac{e}{\hbar} \frac{Ba^2 \sqrt{3}}{2} m & m' = m, n' = n \pm 2, \\ \pm \frac{e}{\hbar} \frac{Ba^2 \sqrt{3}}{4} (m \mp \frac{1}{2}) & m' = m \mp 1, n' = n \pm 1, \\ \pm \frac{e}{\hbar} \frac{Ba^2 \sqrt{3}}{2} (m \mp 1) & m' = m \mp 2, n' = n \pm 2, \\ \pm \frac{e}{\hbar} \frac{Ba^2 \sqrt{3}}{4} (m \mp \frac{3}{2}) & m' = m \mp 3, n' = n \pm 1. \end{cases} \quad (2.27)$$

Identifying $\frac{Ba^2 \sqrt{3}}{2}$ as the magnetic flux Φ passing through per unit cell and $\frac{\hbar}{e}$ corresponds to the magnetic flux quantum Φ_0 , we obtain the following relation:

$$\begin{aligned} H_{jj'}(\mathbf{k}) = & \mathcal{E}_{jj'}(\mathbf{0}) + e^{i\mathbf{k} \cdot \mathbf{R}_1} \mathcal{E}_{jj'}(\mathbf{R}_1) + e^{-i\pi(m+1/2)\Phi/\Phi_0} e^{i\mathbf{k} \cdot \mathbf{R}_2} \mathcal{E}_{jj'}(\mathbf{R}_2) \\ & + e^{-i\pi(m-1/2)\Phi/\Phi_0} e^{i\mathbf{k} \cdot \mathbf{R}_3} \mathcal{E}_{jj'}(\mathbf{R}_3) + e^{i\mathbf{k} \cdot \mathbf{R}_4} \mathcal{E}_{jj'}(\mathbf{R}_4) \\ & + e^{i\pi(m-1/2)\Phi/\Phi_0} e^{i\mathbf{k} \cdot \mathbf{R}_5} \mathcal{E}_{jj'}(\mathbf{R}_5) + e^{i\pi(m+1/2)\Phi/\Phi_0} e^{i\mathbf{k} \cdot \mathbf{R}_6} \mathcal{E}_{jj'}(\mathbf{R}_6) \\ & + e^{-i\pi(m+3/2)\Phi/\Phi_0} e^{i\mathbf{k} \cdot \tilde{\mathbf{R}}_1} \mathcal{E}_{jj'}(\tilde{\mathbf{R}}_1) + e^{-2i\pi m \Phi/\Phi_0} e^{i\mathbf{k} \cdot \tilde{\mathbf{R}}_2} \mathcal{E}_{jj'}(\tilde{\mathbf{R}}_2) \\ & + e^{-i\pi(m-3/2)\Phi/\Phi_0} e^{i\mathbf{k} \cdot \tilde{\mathbf{R}}_3} \mathcal{E}_{jj'}(\tilde{\mathbf{R}}_3) + e^{i\pi(m-3/2)\Phi/\Phi_0} e^{i\mathbf{k} \cdot \tilde{\mathbf{R}}_4} \mathcal{E}_{jj'}(\tilde{\mathbf{R}}_4) \\ & + e^{2i\pi m \Phi/\Phi_0} e^{i\mathbf{k} \cdot \tilde{\mathbf{R}}_5} \mathcal{E}_{jj'}(\tilde{\mathbf{R}}_5) + e^{i\pi(m+3/2)\Phi/\Phi_0} e^{i\mathbf{k} \cdot \tilde{\mathbf{R}}_6} \mathcal{E}_{jj'}(\tilde{\mathbf{R}}_6) \\ & + e^{i\mathbf{k} \cdot \mathbf{R}'_1} \mathcal{E}_{jj'}(\mathbf{R}'_1) + e^{-2i\pi(m+1)\Phi/\Phi_0} e^{i\mathbf{k} \cdot \mathbf{R}'_2} \mathcal{E}_{jj'}(\mathbf{R}'_2) \\ & + e^{-2i\pi(m-1)\Phi/\Phi_0} e^{i\mathbf{k} \cdot \mathbf{R}'_3} \mathcal{E}_{jj'}(\mathbf{R}'_3) + e^{i\mathbf{k} \cdot \mathbf{R}'_4} \mathcal{E}_{jj'}(\mathbf{R}'_4) \\ & + e^{2i\pi(m-1)\Phi/\Phi_0} e^{i\mathbf{k} \cdot \mathbf{R}'_5} \mathcal{E}_{jj'}(\mathbf{R}'_5) + e^{2i\pi(m+1)\Phi/\Phi_0} e^{i\mathbf{k} \cdot \mathbf{R}'_6} \mathcal{E}_{jj'}(\mathbf{R}'_6). \end{aligned} \quad (2.28)$$

The Hamiltonian depends only on the site index m and does not invariant under the expansion of a lattice vector along the x axis. In order to restore this invariance, we can look at the case where the ratio of magnetic flux and flux quanta is a rational number $\Phi/\Phi_0 = p/q$. The crucial advantage of the Peierls phase approach is allowed the lattice periodicity can be restored provided a suitable magnetic unit cell or “magnetic supercell” containing several original unit cells is constructed. One might ask what truly happens inside the magnetic unit cells. Do the neighbor interactions remain the same way as they did in the tight-binding model? We will explore this after deriving the Hamiltonian for the magnetic unit cell.

The magnetic unit cell has lattice vectors $q\mathbf{a}_1$ and \mathbf{a}_2 are illustrated in Fig. (2.5)

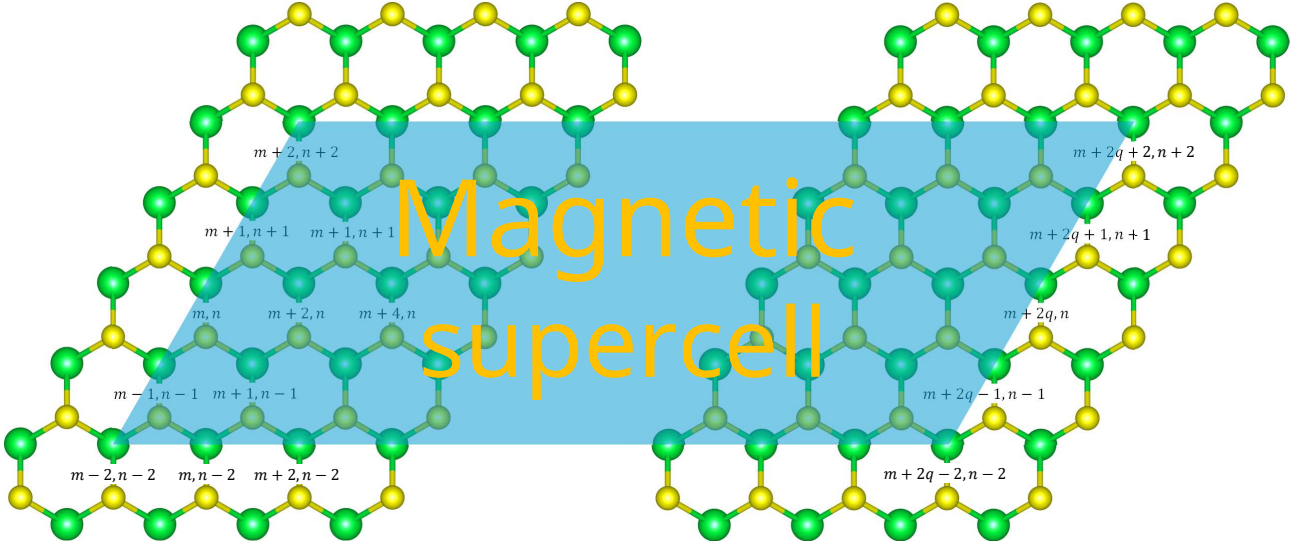


Figure 2.5: Magnetic unit cell for TMD monolayers.

In Section 2.1, we have ignored the sum over of relative positions \mathbf{r}_c in Eq (2.2) due to ignore the orbitals of X atoms. While, the magnetic unit cell consists $2q$ atom M. We, now, define a new basis set of $6q$ atomic orbitals $\{\phi_j(\mathbf{r} - \mathbf{r}_i)\}$ where $j = 1, 2, 3$ and $i = 1, 2, \dots, 2q$. The new basis function now is

$$\psi_{\lambda, \mathbf{k}}(\mathbf{r}) = \sum_j^3 \sum_i^{2q} C_{ji}^{\lambda}(\mathbf{k}) \sum_{\alpha}^{N_{UC}} e^{i\mathbf{k} \cdot (\mathbf{R}_{\alpha} + \mathbf{r}_i)} \phi_j(\mathbf{r} - \mathbf{R}_{\alpha} - \mathbf{r}_i). \quad (2.29)$$

Here, we set \mathbf{r}_i refers to the position of an atom in a unit cell, while \mathbf{R}_{α} denotes the position of different unit cells. The Hamiltonian matrix elements in the new basis is written as

$$H_{jj'}^{ii'}(\mathbf{k}) = \sum_{\alpha}^{N_{UC}} \sum_{\beta}^{N_{UC}} e^{i\mathbf{k} \cdot (\mathbf{R}_{\beta} - \mathbf{R}_{\alpha} + \mathbf{r}_{i'} - \mathbf{r}_i)} \langle \phi_j(\mathbf{r} - \mathbf{R}_{\alpha} - \mathbf{r}_i) | \left[-\frac{\hbar^2 \nabla^2}{2m} + U_0 \right] | \phi_j(\mathbf{r} - \mathbf{R}_{\beta} - \mathbf{r}_{i'}) \rangle. \quad (2.30)$$

Now we center our system at $\mathbf{r}' = \mathbf{r} - \mathbf{R}_{\alpha} - \mathbf{r}_i$ and define $\mathbf{R}_{\gamma} = \mathbf{R}_{\alpha} - \mathbf{R}_{\beta}$. This leads to

$$H_{jj'}^{ii'}(\mathbf{k}) = \sum_{\alpha}^{N_{UC}} \sum_{\gamma}^{N_{UC}} e^{-i\mathbf{k} \cdot (\mathbf{R}_{\gamma} + \mathbf{r}_i - \mathbf{r}_{i'})} \langle \phi_j(\mathbf{r}) | \left[-\frac{\hbar^2 \nabla^2}{2m} + U_0 \right] | \phi_j(\mathbf{r} + \mathbf{R}_{\gamma} + \mathbf{r}_i - \mathbf{r}_{i'}) \rangle. \quad (2.31)$$

Taking the sum over \mathbf{R} and replacing $\mathbf{r}_i = \left(m \frac{a}{2}, n \frac{a\sqrt{3}}{2}\right)$, $\mathbf{r}_{i'} = \left(m' \frac{a}{2}, n' \frac{a\sqrt{3}}{2}\right)$, notice that $i = (m, n)$ with only considering the NN, NNN and TNN, we define our hopping terms

in the new basis is given by

$$H_{jj'}^{ii'}(\mathbf{k}) = \sum_{\alpha}^{N_{\text{UC}}} \sum_{\gamma}^{N_{\text{UC}}} e^{-i\mathbf{k} \cdot \mathbf{R}_{\gamma}} \langle \phi_j(\mathbf{r}) | \left[-\frac{\hbar^2 \nabla^2}{2m} + U_0(\mathbf{r}) \right] | \phi_{j'}(\mathbf{r} + \mathbf{R}_{\gamma}) \rangle \delta_{i,i'}. \quad (2.32)$$

One can recognize that Eq. (2.32) resembles Eq. (2.6). Additionally, the equation not only describes the hopping between magnetic unit cells but also accounts for hopping between sites within magnetic unit cells. To address the previous question, it is important to note that we have enlarged the original unit cell into a magnetic unit cell, which now contains $2q$ atoms M. The neighbor interactions are preserved inside the “supercell”, but they now involve neighboring magnetic unit cells due to the enlarged cell structure. The Hamiltonian has a discrete translational invariance with a unit cell carrying $2q$ unit cells along the x axis.

The last step is to develop the matrix Hamiltonian elements. This can be obtained by taking the sum over \mathbf{R} in Eq. (2.32). We can choose $\mathbf{R}_{\alpha} = \mathbf{0}$, this will not affect the Hamiltonian. In fact, the sum over \mathbf{R} is only considering the NN, NNN, TNN atoms, and replacing \mathbf{R} is equivalent to redefining dummy variables in the equation, Hamiltonian with the Peierls phase now is

$$H_{jj'}^{ii'}(\mathbf{k}) = \sum_{\beta}^{N_{\text{UC}}} e^{i\mathbf{k} \cdot \mathbf{R}_{\beta}} \langle \phi_j(\mathbf{r}) | \left[-\frac{\hbar^2 \nabla^2}{2m} + U_0(\mathbf{r}) \right] | \phi_{j'}(\mathbf{r} - \mathbf{R}_{\beta}) \rangle \delta_{i,i'}. \quad (2.33)$$

Simplifying Eq. (2.33), we get the Hamiltonian for the magnetic unit cell

$$\begin{aligned} H_{jmjn'm'n'}(\mathbf{k}) = & \mathcal{E}_{jj'}(\mathbf{0}) \delta_{m,m'}^{n,n'} + e^{i\mathbf{k} \cdot \mathbf{R}_1} \mathcal{E}_{jj'}(\mathbf{R}_1) \delta_{m+2,m'}^{n,n'} + e^{i\mathbf{k} \cdot \mathbf{R}_4} \mathcal{E}_{jj'}(\mathbf{R}_4) \delta_{m-2,m'}^{n,n'} \\ & + e^{-i\pi(m+1/2)p/q} e^{i\mathbf{k} \cdot \mathbf{R}_2} \mathcal{E}_{jj'}(\mathbf{R}_2) \delta_{m+1,m'}^{n-1,n'} + e^{-i\pi(m-1/2)p/q} e^{i\mathbf{k} \cdot \mathbf{R}_3} \mathcal{E}_{jj'}(\mathbf{R}_3) \delta_{m-1,m'}^{n-1,n'} \\ & + e^{i\pi(m-1/2)p/q} e^{i\mathbf{k} \cdot \mathbf{R}_5} \mathcal{E}_{jj'}(\mathbf{R}_5) \delta_{m-1,m'}^{n+1,n'} + e^{i\pi(m+1/2)p/q} e^{i\mathbf{k} \cdot \mathbf{R}_6} \mathcal{E}_{jj'}(\mathbf{R}_6) \delta_{m+1,m'}^{n+1,n'} \\ & + e^{-i\pi(m+3/2)\Phi/\Phi_0} e^{i\mathbf{k} \cdot \tilde{\mathbf{R}}_1} \mathcal{E}_{jj'}(\tilde{\mathbf{R}}_1) \delta_{m+3,m'}^{n-1,n'} + e^{-2i\pi m\Phi/\Phi_0} e^{i\mathbf{k} \cdot \tilde{\mathbf{R}}_2} \mathcal{E}_{jj'}(\tilde{\mathbf{R}}_2) \delta_{m,m'}^{n-2,n'} \\ & + e^{-i\pi(m-3/2)\Phi/\Phi_0} e^{i\mathbf{k} \cdot \tilde{\mathbf{R}}_3} \mathcal{E}_{jj'}(\tilde{\mathbf{R}}_3) \delta_{m-3,m'}^{n-1,n'} + e^{i\pi(m-3/2)\Phi/\Phi_0} e^{i\mathbf{k} \cdot \tilde{\mathbf{R}}_4} \mathcal{E}_{jj'}(\tilde{\mathbf{R}}_4) \delta_{m-3,m'}^{n+1,n'} \quad (2.34) \\ & + e^{2i\pi m\Phi/\Phi_0} e^{i\mathbf{k} \cdot \tilde{\mathbf{R}}_5} \mathcal{E}_{jj'}(\tilde{\mathbf{R}}_5) \delta_{m,m'}^{n+2,n'} + e^{i\pi(m+3/2)\Phi/\Phi_0} e^{i\mathbf{k} \cdot \tilde{\mathbf{R}}_6} \mathcal{E}_{jj'}(\tilde{\mathbf{R}}_6) \delta_{m+3,m'}^{n+1,n'} \\ & + e^{i\mathbf{k} \cdot \mathbf{R}'_1} \mathcal{E}_{jj'}(\mathbf{R}'_1) \delta_{m+4,m'}^{n,n'} + e^{-2i\pi(m+1)\Phi/\Phi_0} e^{i\mathbf{k} \cdot \mathbf{R}'_2} \mathcal{E}_{jj'}(\mathbf{R}'_2) \delta_{m+2,m'}^{n-2,n'} \\ & + e^{-2i\pi(m-1)\Phi/\Phi_0} e^{i\mathbf{k} \cdot \mathbf{R}'_3} \mathcal{E}_{jj'}(\mathbf{R}'_3) \delta_{m-2,m'}^{n-2,n'} + e^{i\mathbf{k} \cdot \mathbf{R}'_4} \mathcal{E}_{jj'}(\mathbf{R}'_4) \delta_{m-4,m'}^{n,n'} \\ & + e^{2i\pi(m-1)\Phi/\Phi_0} e^{i\mathbf{k} \cdot \mathbf{R}'_5} \mathcal{E}_{jj'}(\mathbf{R}'_5) \delta_{m-2,m'}^{n+2,n'} + e^{2i\pi(m+1)\Phi/\Phi_0} e^{i\mathbf{k} \cdot \mathbf{R}'_6} \mathcal{E}_{jj'}(\mathbf{R}'_6) \delta_{m+2,m'}^{n+2,n'}. \end{aligned}$$

Now, for given flux ratio p/q , only the q determines the periodicity of the magnetic cell assuming p and q are mutually prime numbers. When we plot the band energies while varying the p , we obtain the famous Hofstadter butterfly [4], a complex fractal

structure as seen in Fig. (2.7). This structure is generated at the K -point. This fractal spectrum is a result of two competing effects, lattice periodicity and magnetic unit cell periodicity enforced by the presence of the magnetic field. Eq. (2.34) give the following matrix which must be diagonalized to obtain the energy eigenvalues

$$H = \begin{pmatrix} V_0 & V_1 & V_2 \\ V_1^* & V_{11} & V_{12} \\ V_2^* & V_{12}^* & V_{22} \end{pmatrix}, \quad (2.35)$$

with

$$H_{jj'} = \begin{pmatrix} A_{jj'}^{(0)} & B_{jj'}^{(0)} & C_{jj}^{(0)} & D_{jj'}^{(0)} & E_{jj'}^{(0)} & F_{jj'}^{(0)} & 0 & \cdots & G_{jj'}^{(0)} & H_{jj'}^{(0)} & I_{jj'}^{(0)} & K_{jj'}^{(0)} \\ K_{jj'}^{(1)} & A_{jj'}^{(1)} & B_{jj'}^{(1)} & C_{jj'}^{(1)} & D_{jj'}^{(1)} & E_{jj'}^{(1)} & F_{jj'}^{(1)} & 0 & \cdots & G_{jj'}^{(1)} & H_{jj'}^{(1)} & I_{jj'}^{(1)} \\ I_{jj'}^{(2)} & K_{jj'}^{(2)} & A_{jj'}^{(2)} & B_{jj'}^{(2)} & C_{jj'}^{(2)} & D_{jj'}^{(2)} & E_{jj'}^{(2)} & F_{jj'}^{(2)} & 0 & \cdots & G_{jj'}^{(2)} & H_{jj'}^{(2)} \\ \vdots & \vdots \\ C_{jj'}^{(q-2)} & \cdots & \cdots & \cdots & \cdots & \cdots & \cdots & 0 & \cdots & K_{jj'}^{(q-2)} & A_{jj'}^{(q-2)} & B_{jj'}^{(q-2)} \\ B_{jj'}^{(q-1)} & C_{jj'}^{(q-1)} & \cdots & 0 & \cdots & K_{jj'}^{(q-1)} & A_{jj'}^{(q-1)} \end{pmatrix}, \quad (2.36)$$

where $A_{jj'}^{(m)}$ is the hopping with the relative coordinates (m, n) , $B_{jj'}^{(m)}$ is the hopping with the relative coordinates $(m+1, n)$, and so on, and $V_0, V_1, V_2, V_{11}, V_{12}, V_{22}$ are submatrices of size $6q \times 6q$, see Fig. (2.6).

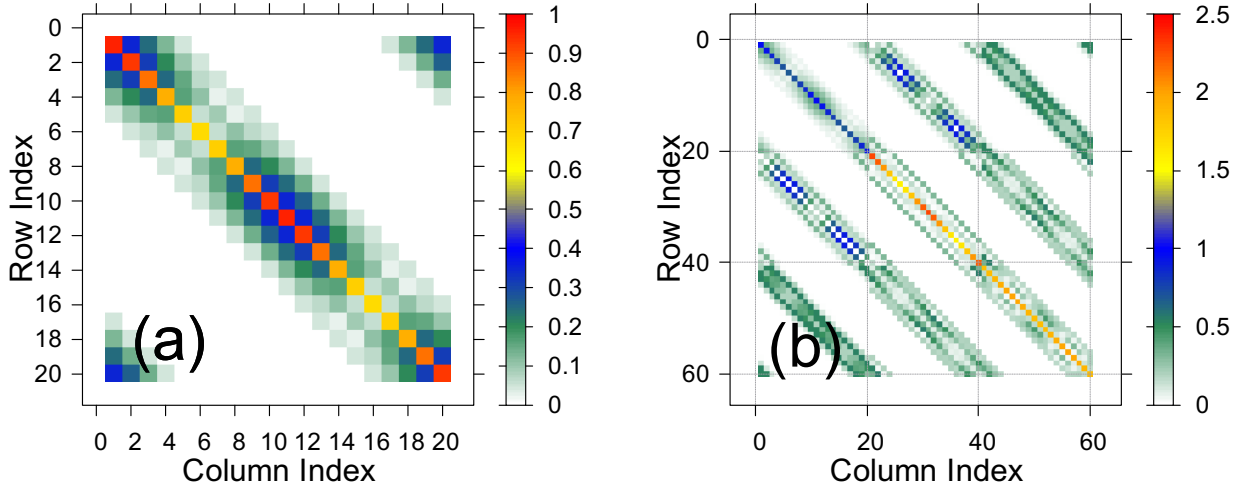


Figure 2.6: A simple and intuitive visualization of sub-matrix h_0 for single-band(a) and matrix H for three band(b) using standard plotter with $q = 20$.

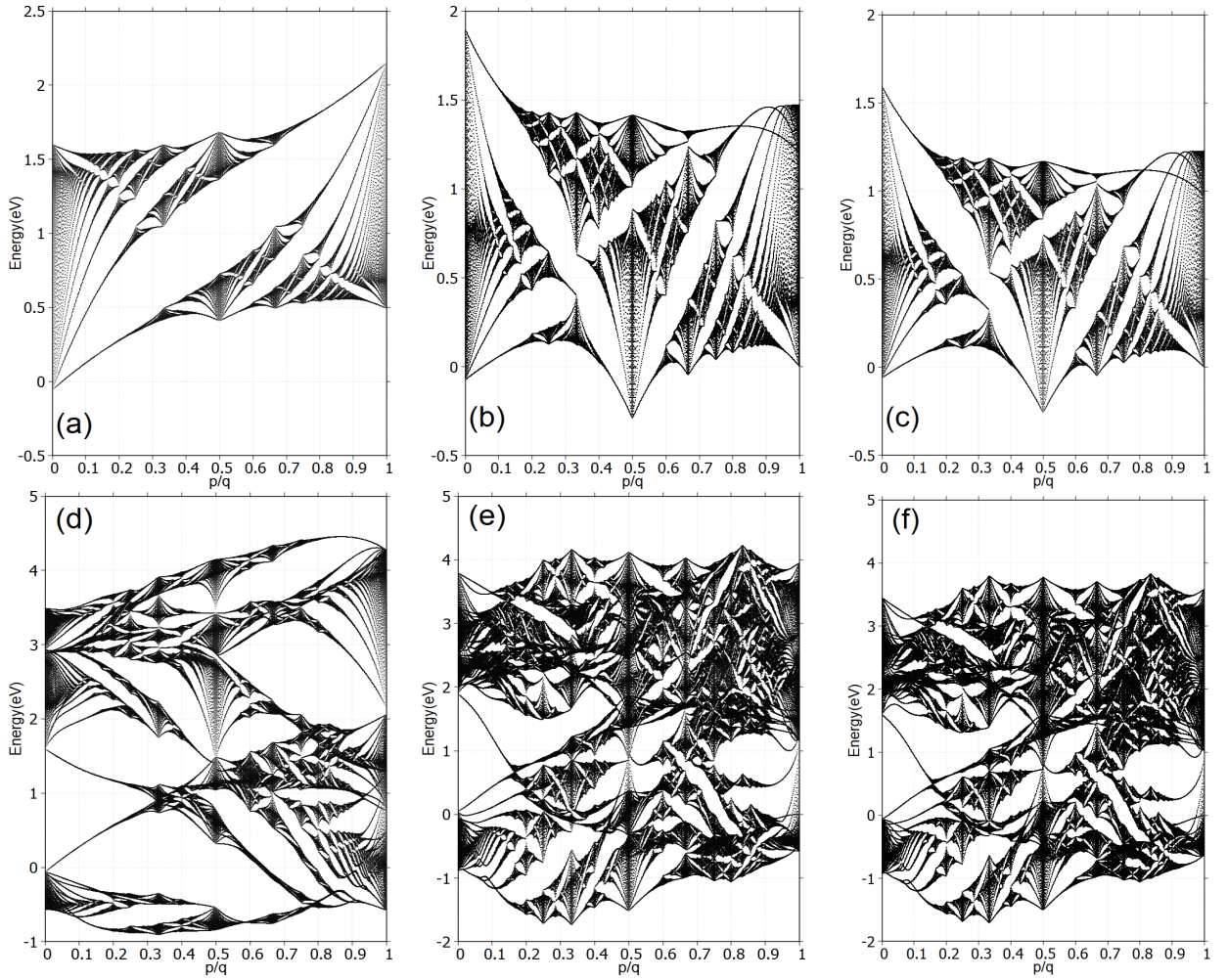


Figure 2.7: Hofstadter butterfly for single-band $|dz\rangle \equiv |\phi_1^1(x, y)\rangle$ (a,b,c) and all band (d,e,f) for NN and TNN for MoS₂, respectively, with $q = 797$ and vary p from 1 to q with field strength $B_0 = 4.6928 \times 10^4$ T. Here on x -axis represents the flux in units of quantum flux enclosed by the unit cell and y -axis represents the Energy. While (b,e) use generalized-gradient approximation (GGA) parameter, (c,f) use local-density approximation (LDA) one.

The magnetic field enters the TB Hamiltonian only through the fraction p/q , which is the magnetic flux through the primitive unit cell of the lattice. In general, as the lattice geometry evolves, the area of the primitive unit cell changes m times.

Another observation is that the lattice constant a and the magnetic field B always appears together in an expression with the magnetic field ($\frac{Ba^2\sqrt{3}}{2}$). This quantity reflects the flux per plaquette in the super magnetic unit cell, which is relevant in the context of Aharonov-Bohm effect [5]. Since the expression involves the product Ba^2 , this implies that increasing B by a certain amount is mathematically equivalent to increasing a . In other words, for energy calculations, increasing the strength of the magnetic field is physically equivalent to increasing the lattice constant, as both affect the system in the same way through the flux per unit cell. In addition, the three-band spectrum contains a complex and rich physics insight but it seems remains the fractal structure.

The main energy bands are basically Landau levels (LLs), which we shall discuss in the next Section. For small values of the magnetic flux ratio p/q , these LLs manifest sharp and well-separated energy bands. However, when increasing p from 1 to q , each LLs go a recursive splitting into q subbands. This structure arises from the magnetic unit cell's periodicity.

The spectrum exhibits several noticeable symmetries. First, it depends only on the flux ratio p/q , meaning that shifting p/q by an integer c (i.e., $p/q \rightarrow p/q + c$) leaves the spectrum unchanged. Additionally, the spectrum remains invariant under the transformation $p/q \rightarrow -p/q$, since if ψ is an eigenstate with energy E for flux p/q , its complex conjugate ψ^* is an eigenstate with the same energy for flux $-p/q$. These two symmetries are general and not specific to the MX_2 case. However, the third symmetry involves changing p/q to $p/q + 1/2$, which is equivalent to flipping the sign of the hopping energies t_i (i.e., $t_i \rightarrow -t_i$), resulting in an inversion of the spectrum, which is concealed clearly in square lattice [4] or honeycomb lattice [6], but in the case MX_2

The role of the eight hopping constants t is just to set an energy scale. Change the hopping constants amounts to stretching the butterfly spectrum vertically, which is an overall scaling to the energy levels. Thus it does not give rise to any interesting physical phenomenon.

Due to the significant mass of the transition-metal atom M, its spin orbit coupling (SOC) can be large. For simplicity, we consider only the on-site contribution, which corresponds to the $\mathbf{L} \cdot \mathbf{S}$ term originating from the M atoms. Using the basis set $\{|d_{z^2}, \uparrow\rangle, |d_{xy}, \uparrow\rangle, |d_{x^2-y^2}, \uparrow\rangle, |d_{z^2}, \downarrow\rangle, |d_{xy}, \downarrow\rangle, |d_{x^2-y^2}, \downarrow\rangle\}$, we derive the SOC term in the Hamiltonian as

$$H' = \lambda \mathbf{L} \cdot \mathbf{S} = \frac{\lambda}{2} \begin{pmatrix} L_z & L_x - iL_y \\ L_x + iL_y & -L_z \end{pmatrix}, \quad (2.37)$$

in which

$$L_z = \begin{pmatrix} 0 & 0 & 0 \\ 0 & 0 & 2i \\ 0 & -2i & 0 \end{pmatrix}, \quad (2.38)$$

is the matrix of \hat{L}_z (z component of the orbital angular momentum) in bases of $d_{z^2}, d_{xy}, d_{x^2-y^2}$ and λ is characterized the strength of the SOC. Noting that, under the three bases, the matrix elements of \hat{L}_x and \hat{L}_y are all zeros. Therefore the full TB Hamiltonian for the

magnetic unit cell with the SOC as follows

$$\begin{aligned}
 H_{\text{SOC}}(\mathbf{k}) &= \mathbf{I}_2 \otimes H(\mathbf{k}) + \mathbf{I}_q \otimes H' \\
 &= \begin{pmatrix} H_{3q \times 3q}(\mathbf{k}) + \frac{\lambda}{2} L_z & 0 \\ 0 & H_{3q \times 3q}(\mathbf{k}) - \frac{\lambda}{2} L_z \end{pmatrix}, \tag{2.39}
 \end{aligned}$$

in which \mathbf{I}_2 is the 2×2 identity matrix.

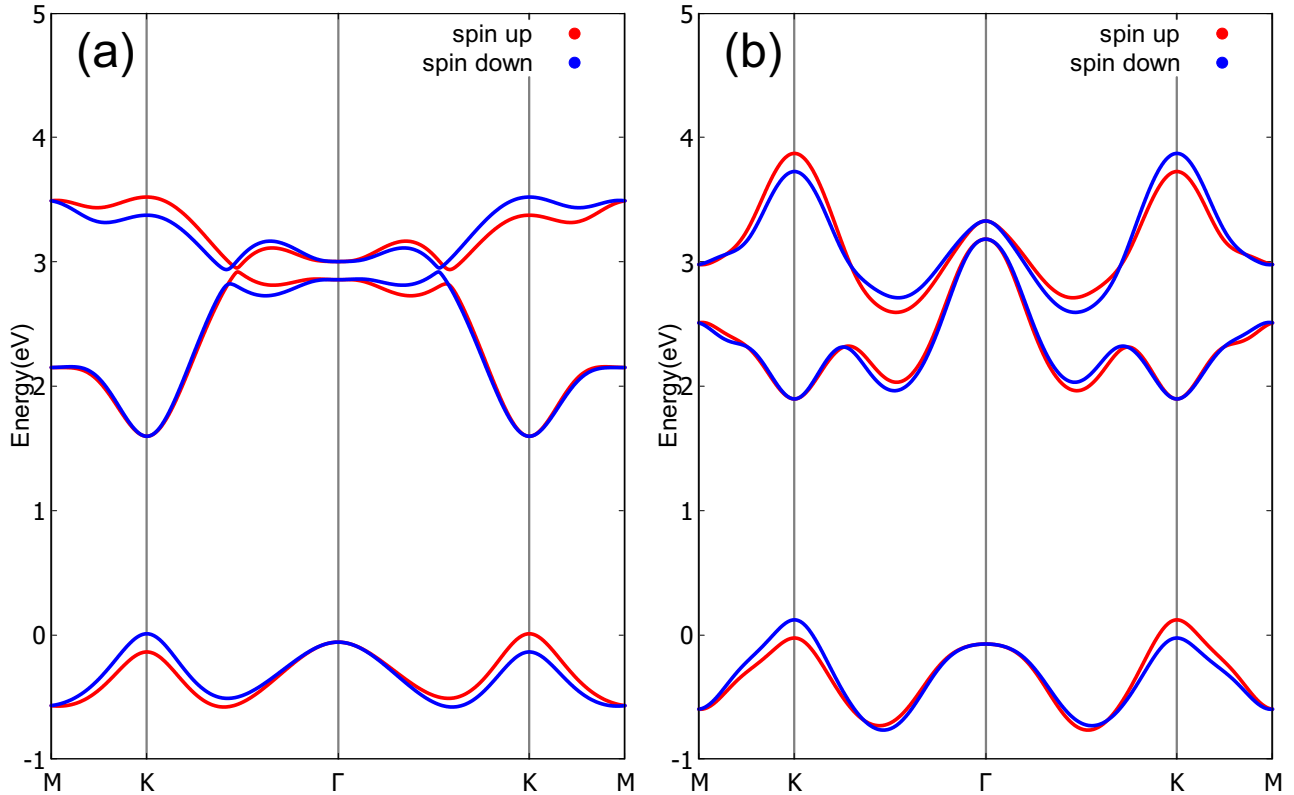


Figure 2.8: Band structure of monolayer MoS₂ along Γ -K direction, SOC causes huge spin splittings in band-structure at K and $-K$ points.

An alternative approach to the derivation of the Hamiltonian under an uniform magnetic field is given in Appendix C.

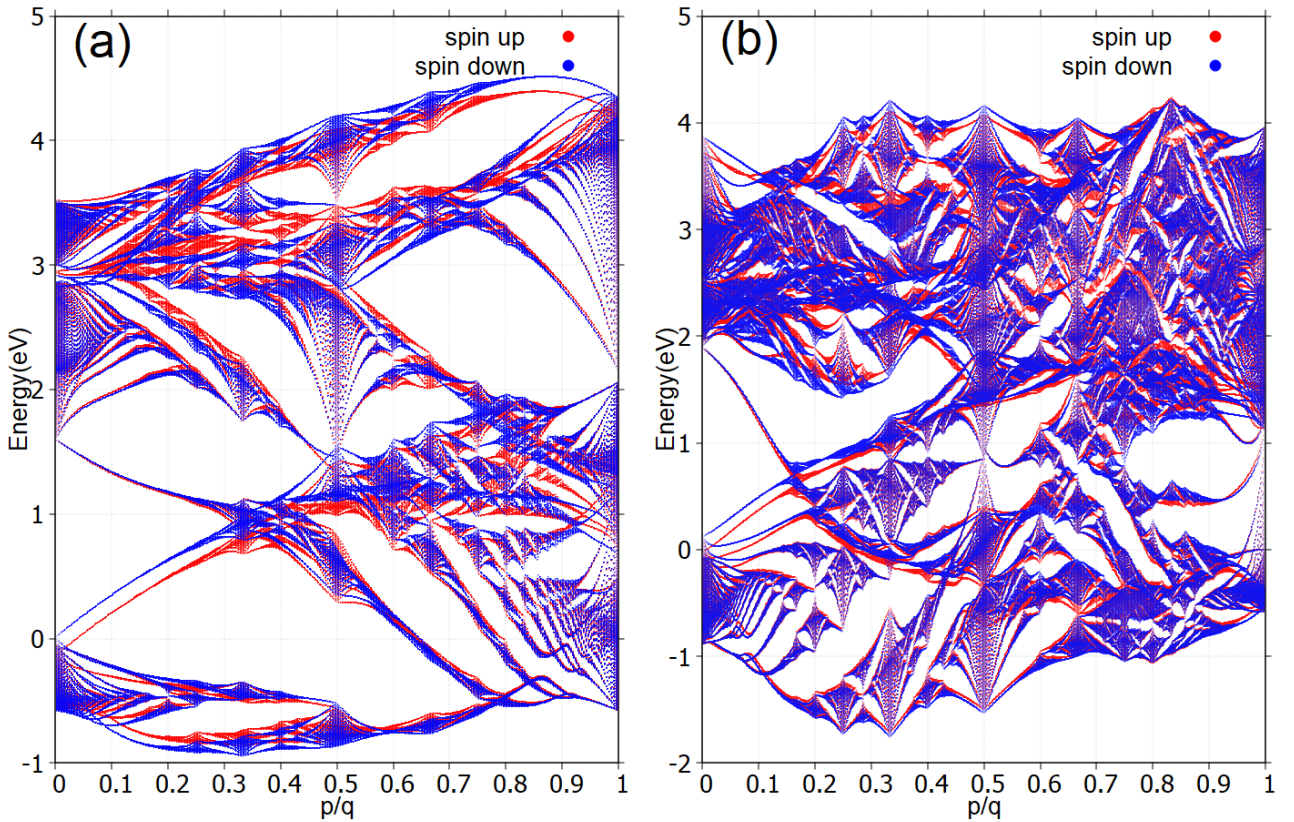


Figure 2.9: Band structure of monolayer MoS₂ along Γ -K direction, SOC causes huge spin splittings in band-structure at K and $-K$ points.

2.3 Landau levels

In solid-state physics, the behavior of electrons in magnetic fields is usually introduced by using the Hamiltonian

$$H = \frac{\mathbf{p} + e\mathbf{A}(\mathbf{r})^2}{2m}, \quad (2.40)$$

and the energy eigenfunctions are known as LLs

$$E_n = (n + 1/2) \hbar\omega_c. \quad (2.41)$$

This treatment is for free electrons, but near the bottom of the two-dimensional tight-binding band of TMD we must find a regime in which the electron behaves as a nearly one(At least with a nearly free dispersion relation).

Recalling the result obtained for the dispersion relation of an electron within the TBM

$$H_{11} = 2t_0(\cos 2\alpha + 2 \cos \alpha \cos \beta) + \epsilon_1, \quad (2.42)$$

The dispersion energy is approximately free-electron-like by Taylor expansion to second

order of \mathbf{k}

$$\begin{aligned} H_{11}(\mathbf{k}) &\approx 2t_0 \left[1 - \frac{a^2 k_x^2}{2} + 2 \left(1 - \frac{a^2 k_x^2}{8} \right) \left(1 - \frac{3a^2 k_y^2}{8} \right) \right] \\ &= t_0 \frac{3}{16} (32 + a^4 k_x^2 k_y^2) - t_0 \frac{3}{2} a^2 (k_x^2 + k_y^2) + \epsilon_1, \end{aligned} \quad (2.43)$$

the term a^4 is negligibly small, then we have

$$H_{11}(\mathbf{k}) \approx 6t_0 - \frac{3}{2} t_0 a^2 (k_x^2 + k_y^2) + \epsilon_1. \quad (2.44)$$

One of the ways derivation of effective mass m^* is substitution $\hbar\mathbf{k} \rightarrow \mathbf{\Pi} + e\mathbf{A}$, with Landau gauge $\mathbf{A} = (0, Bx, 0)$

$$\begin{aligned} H_{11}(\mathbf{\Pi}) &\approx 6t_0 - \frac{3}{2} t_0 \frac{a^2}{\hbar^2} \left[\Pi_x^2 + (\Pi_y + eBx)^2 \right] + \epsilon_1 \\ &\approx 6t_0 - \frac{3}{2} t_0 \frac{a^2}{\hbar^2} \Pi_x^2 - \frac{3}{2} t_0 \frac{a^2}{\hbar^2} (eB)^2 \left[x - \left(-\frac{\hbar k_y}{eB} \right) \right]^2 + \epsilon_1. \end{aligned} \quad (2.45)$$

The Eq (2.45) can be rewrite in the form as

$$E(\mathbf{\Pi}) = 6t_0 - \left[\frac{1}{2m^*} \Pi_x^2 + \frac{1}{2} m^* \omega_c^2 (x - x_0)^2 \right] + \epsilon_1, \quad (2.46)$$

where $m^* = \frac{\hbar^2}{3t_0 a^2}$ is the effective mass and $x_0 = \frac{\hbar k_y}{eB}$. Subsequently, the cyclotron frequency is

$$\omega_c = \frac{eB}{m^*} = \frac{8\pi\sqrt{3}t_0}{\hbar} \frac{p}{q}, \quad (2.47)$$

and therefore the Landau levels near the bottom of the band structure can be written as

$$\begin{aligned} E_n &= 6t_0 - \hbar\omega_c(n + 1/2) + \epsilon_1 \\ &= t_0 \left(6 - 8\pi\sqrt{3} \frac{p}{q} (n + 1/2) \right) + \epsilon_1, \end{aligned} \quad (2.48)$$

in linear order of an uniform-flux, where n is Landau index. These levels give rise to what is called “the Landau fan”, being very important in the de Haas-van Alphen and Shubnikov-de Haas effects [7] which predicts oscillations of the magnetic moment of a metal depending on an applied magnetic field.

In Fig 2.12 we compare the spectrum of a small section of single-band with $p/q = 1/797$, which is equivalent to small magnetic field, the spectrum of MoS₂, with the energy of Landau levels given by Eq. (2.48) show standard equally spaced LLs [8–11]

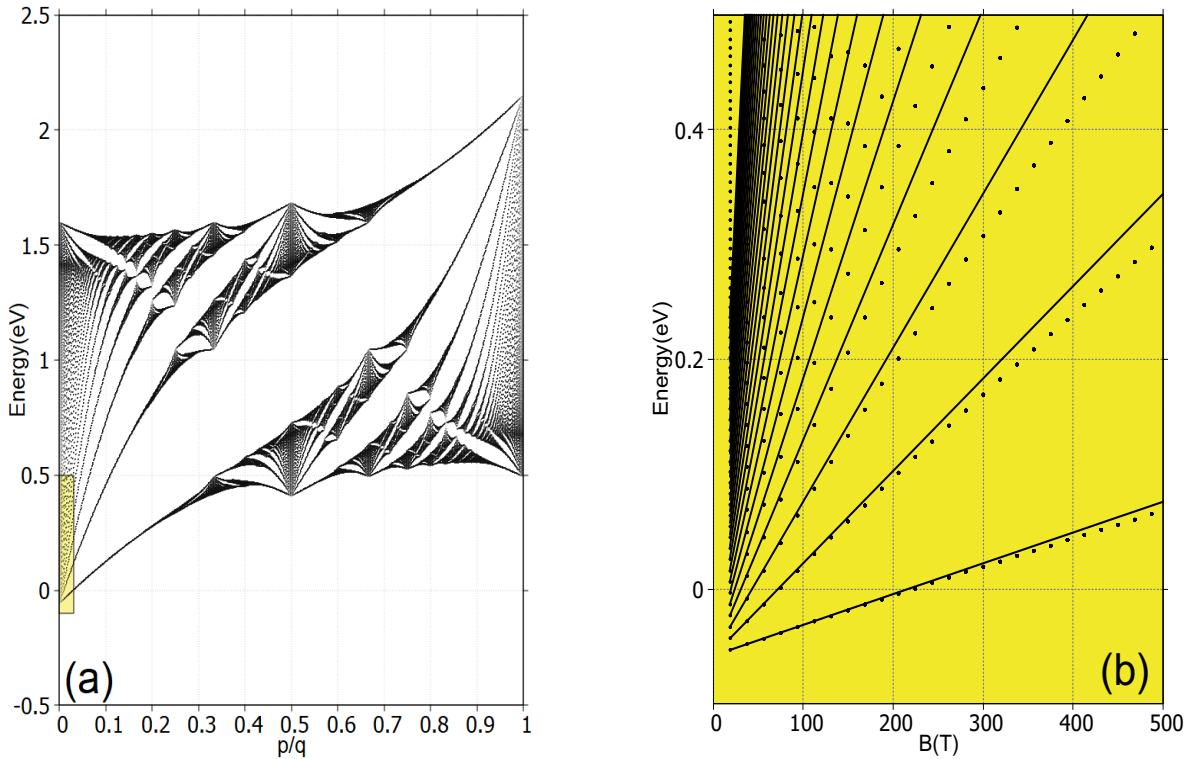


Figure 2.10: (a) Same plot as Fig (2.7a) but considering a small area and (b) shows superposition of the Landau fan diagram and the Hofstadter butterfly. Display the first $n = 30$ levels near the bottom of the conduction band for a magnetic field up to $B = 500$ T.

near the bottom of the bands, as plotted in Fig 2.12(b). The fan of LLs can be clearly seen emerging from the pattern in Fig 2.12(a).

In Fig 2.12(a), there is just single-band in case zero field, with the effective mass $m^* = \frac{\hbar}{3t_0a^2}$. The numerical result for this portion of the spectrum are shown in Fig 2.12 for $p/q \geq 1/797$. The first few LLs are clearly seen, and the asymptotic slopes p/q at large q given by Eq. (2.48) are shown for comparison for the first five Landau levels at $B \leq 100$ T. At the values of B the fit is not ideal, but it does seem to be improving with the decreasing p/q .

Figure 2.12 also displays a blowup of the low uniform magnetic region and the LLs as a function of Φ/Φ_0 [12]. The Landau levels are all close to being linear in B , resulting from the magnetic quantization of parabolic bands at $B = 0$ T i.e. increasing values of B , these LLs are sequentially depleted; for $B = 200$ T the levels are completely filled up to the level $n = 4$; for $B = 500$ T it happens the same, only this time are filled up to the level $n = 1$ and so on.

2.4 Hall effects

2.4.1 The classical Hall effect

The appearance of LLs leads to a quantized Hall conductance. Before delving into the quantum Hall effect, let us start by taking a look at its classical counterpart i.e., the Hall effect. The Hall effect arises when a conductor carrying an electric current is placed in an external magnetic field \mathbf{B} . The Lorentz force from the magnetic field causes the charges to accumulate on one side of the conductor. Starting with an electric field \mathbf{E} established in the solid results in a current density \mathbf{J} linearly related to the field through Ohm's law

$$\mathbf{J} = \boldsymbol{\sigma} \mathbf{E}, \quad (2.49)$$

$$\mathbf{E} = \sigma^{-1} \mathbf{J} = \rho \mathbf{J}, \quad (2.50)$$

where $\boldsymbol{\sigma}$ is the conductivity tensor and the resistivity ρ is defined as the inverse of the conductivity. This remains true when both are tensors

$$\begin{pmatrix} J_x \\ J_y \end{pmatrix} = \begin{pmatrix} \sigma_{xx} & \sigma_{xy} \\ \sigma_{yx} & \sigma_{yy} \end{pmatrix} \begin{pmatrix} E_x \\ E_y \end{pmatrix}, \quad (2.51)$$

$$\begin{pmatrix} E_x \\ E_y \end{pmatrix} \begin{pmatrix} \rho_{xx} & \rho_{xy} \\ \rho_{yx} & \rho_{yy} \end{pmatrix} \begin{pmatrix} J_x \\ J_y \end{pmatrix}. \quad (2.52)$$

The off-diagonal components of resistivity tensor is $\rho_{xy} = \rho_{yx} = \frac{B}{en}$. Usually we measure the resistance R , which differs from the resistivity ρ by geometric factors. However, for ρ_{xy} , this thing coincide. To see this, consider a sample of material of length L in the y -direction. We drop a voltage V_y in the y -direction and measure the resulting current I_x in the x -direction. The transverse resistance is

$$R_{xy} = \frac{V_y}{I_x} = \frac{LE_y}{LJ_x} = \frac{E_y}{J_x} = -\rho_{xy}. \quad (2.53)$$

For a current I_x flowing in the x -direction, and the corresponded electric field E_y in the y -direction, the Hall coefficient is defined by

$$R_H = \frac{\rho_{xy}}{B} = \frac{1}{en}. \quad (2.54)$$

showing the Hall resistance is a constant in the classical regime. We see that the Hall coefficient depends only on microscopic information about the material: the charge and density of conduction particles. The Hall coefficient does not depend on the scattering

time τ ; it remains unaffected by the specific frictional mechanism present in the material.

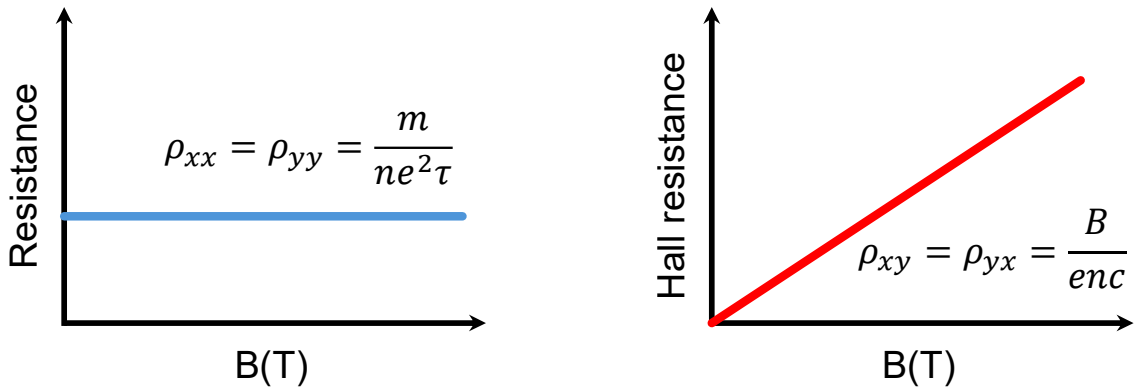


Figure 2.11: The longitudinal resistance on the right figure and the Hall resistance in the left figure. The graph shows both the longitudinal resistance and the Hall resistance is linear to the increasing magnetic field.

2.4.2 The Quantum Hall effect

In previous section, we arrived at the classical Hall resistance, which remains stable under the classical mechanics framework. However, our world is governed not only by classical physics but also by quantum mechanics. Things changes significantly at extremely low temperatures and strong magnetic fields, revealing new quantum phenomena.

There are two related phenomena which are associated to two different quantum Hall effects. These are called the integer Quantum Hall effect (IQHE) and fractional Quantum Hall effect (FQHE). In this study, we mainly focus on the IQHE where the flux number and flux quanta are integers. This phenomenon can be understood without taking into account the Coulomb interaction between electrons, which means we shall continue using the single electron Hamiltonian that we described in Section 2. In this section, we first discovered and subsequently understood theoretically the integer quantum Hall effect in the Hofstadter butterfly.

In two dimensional, there is a crucial relationship between the conductivity tensor σ and the resistivity tensor ρ is given by

$$\begin{bmatrix} \sigma_{xx} & \sigma_{xy} \\ \sigma_{yx} & \sigma_{yy} \end{bmatrix} \begin{bmatrix} \rho_{xx} & \rho_{xy} \\ \rho_{yx} & \rho_{yy} \end{bmatrix}^{-1} = \frac{1}{\rho_{xx}\rho_{yy} - \rho_{xy}\rho_{yx}} \begin{bmatrix} \rho_{yy} & -\rho_{xy} \\ -\rho_{yx} & \rho_{xx} \end{bmatrix}. \quad (2.55)$$

Let's take a look at the experimental data for the quantum Hall effect were performed in 1980 by von Klitzing *et al.* [13]

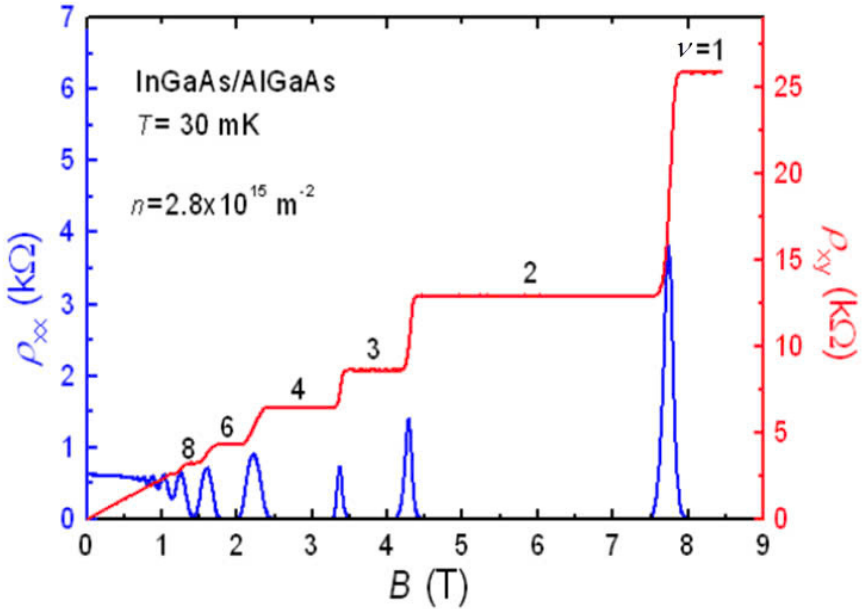


Figure 2.12: This is the integer quantum Hall effect. For this Klaus von Klitzing was awarded the 1985 Nobel prize.

Both the Hall resistivity ρ_{xy} and the longitudinal resistivity ρ_{xx} depict fascinating behaviour. Perhaps the most striking feature in the figure is the fact that the Hall resistivity ρ_{xy} sits on a plateau for a range of magnetic field, before jumping dramatically to the next plateau, while the longitudinal spikes sharply at the transitions between plateaux but vanishes on the plateaux themselves.

The Hall resistivity is now defined

$$\rho_{xy} = \frac{R_K}{\nu}, \quad \nu = 1, 2, \dots \quad (2.56)$$

while ν is the total filled Landau levels and R_K is Klitzing's resistance constant

$$R_K = \frac{h}{e^2} = 25812.8074555\Omega \pm 0.0000059\Omega. \quad (2.57)$$

Between two plateaux, if $\rho_{xy} = 0$ then we get the familiar relation between resistivity and conductivity is $\sigma_{xx} = 1/\rho_{xx}$. But on these Hall plateaux

$$\rho_{xy} = \rho_{yx} = \text{const}, \quad \rho_{xx} = \rho_{yy} = 0, \quad (2.58)$$

this leads to

$$\sigma_{xy} = \sigma_{yx} = 1/\text{const}, \quad \sigma_{xx} = \sigma_{yy} = 0. \quad (2.59)$$

There is an apparent paradox here, we would call a system with $\rho_{xx} = 0$ is a perfect

conductor, while one with $\sigma_{xx} = 0$ is a perfect insulator. But what if both $\rho_{xx} = 0$ and $\sigma_{xx} = 0$ occur simultaneously? A new material or a new state of matter?

2.4.3 Color the Hofstadter butterfly

The contribution to the Hall conductivity from a single subband is given by [14–17]

$$\sigma_{xy} = \frac{e^2}{h} \sum_n^{\text{occ.}} \frac{1}{2\pi} \iint_{\text{BZ}} dk_x dk_y \Omega_n^z(\mathbf{k}). \quad (2.60)$$

In general, the Berry curvature integrated over a closed manifold is quantized in the units of e^2/h and equals to the net number of monopoles inside. This number is called the Chern number and is responsible for a number of quantization effects. Therefore the Hall conductivity is quantized for a two dimensional band insulator of noninteracting electrons. Since the integral for the whole Brillouin zone respectively Berry curvature, we arrived at the Thouless-Kohmoto-Nightingale-Nijs (TKNN)’s formula [17]

$$\sigma_{xy} = \frac{e^2}{h} \nu, \quad \nu = 1, 2, \dots \quad (2.61)$$

ν is guaranteed to be an integer given by the Chern number.

We, then, calculate the quantum Hall conductivity by the Streda formula [18]

$$\sigma_{xy}(B, E_F) = e \frac{\partial N(E, B)}{\partial B} \bigg|_{E=E_F}, \quad (2.62)$$

where $N(E_F, B)$ is the number of state at fixed Fermi energy E_F . Combining Eq. (2.61) and Eq. (2.62), we have

$$\frac{\partial N}{\partial B} = \frac{e}{h} \nu. \quad (2.63)$$

Assuming that B vary slightly

$$N = c + \frac{e}{h} B \nu, \quad c \text{ is any constant.} \quad (2.64)$$

Before this, we have defined $\frac{p}{q} = \frac{eB a^2 \sqrt{3}}{2h}$, with $S = \frac{\sqrt{3}a^2}{2}$ is the area of the original unit cell in Section 2.2. Multiply S with Eq. (2.64), we have

$$N \times S = c + \frac{p}{q} \nu, \quad (2.65)$$

and the density of electron in a single band is given by $\frac{1}{Sq}$, thus when there are r bands

below the Fermi energy level, the density of electron for r^{th} band is

$$N = \frac{r}{Sq}. \quad (2.66)$$

Then, the Eq. (2.66), is written as,

$$r = c \times q + p \times \nu_r, \quad (2.67)$$

in this equation r, q, p, ν are integers, thus, $c \times q$ must be an integer. On the one hand, since c is independent of q , then c itself must be an integer, namely s_r . Thus we have

$$r = q \times s_r + p \times \nu_r, \quad (2.68)$$

this equation is usually named as the Diophantine equation. While ν_r is the Chern number associated with the quantized Hall conductance which can be found by taking ν_r between $-q/2$ and $q/2$ and determining its allows conductance to be determined, s is another integer that play a role in indentify the gap index.

The Hall conductivity of the lattice model for an electron in a background magnetic field can only be computed when the flux ratio $\frac{\Phi}{\Phi_0} = \frac{p}{q}$ is rational. In this case, we can use the TKNN formula, but with the Chern number, which used to be defined by intergrating over the Brillouin zone, now arising by intergrating over the magnetic Brillouin zone. Others derivation is in [1, 19, 20].

The Diophantine equation is crucial in understanding the quantization of Hall conductance in the Hofstadter butterfly. The Chern number ν determines the topological nature of the bands and their contribution to the Hall conductance, while the integer s identifies specific energy gaps in the spectrum. These gaps are directly linked to incompressible quantum Hall states, which are of significant interest in both theoretical and experimental condensed matter physics. The solutions to the Diophantine equation are presented in Table (C.1) in Appendix C, revealing many interesting observations can be extracted from it. Firstly, we observe the occurence values of $\nu = \pm 1$ at both $r = p$ and $r = q - p$. This owing to each band being devided into q subbands. Significantly, the case $r = p$, where the corresponding gap index naturally corresponds to the first gap in the Landau level. The second observation is the symmetry of the table, the value of ν_r is equal to $-\nu_{q-r}$. This is due, once again, to the symmetry of the butterfly.

To further explore the intricate fractal nature of the Hofstadter spectrum, we shall now achieve the colored Hofstadter butterfly. There are many ways to color the butterfly. For instance, a common approach is to color each point of the butterfly based

on their Chern number, as illustrated in the Fig 2.14. At these points, the Hall conductivity highlights exactly quantization. However, a drawback of this method is that the butterfly may contain a dense of points, which can make it difficult to visualise fine details in the colored spectrum.

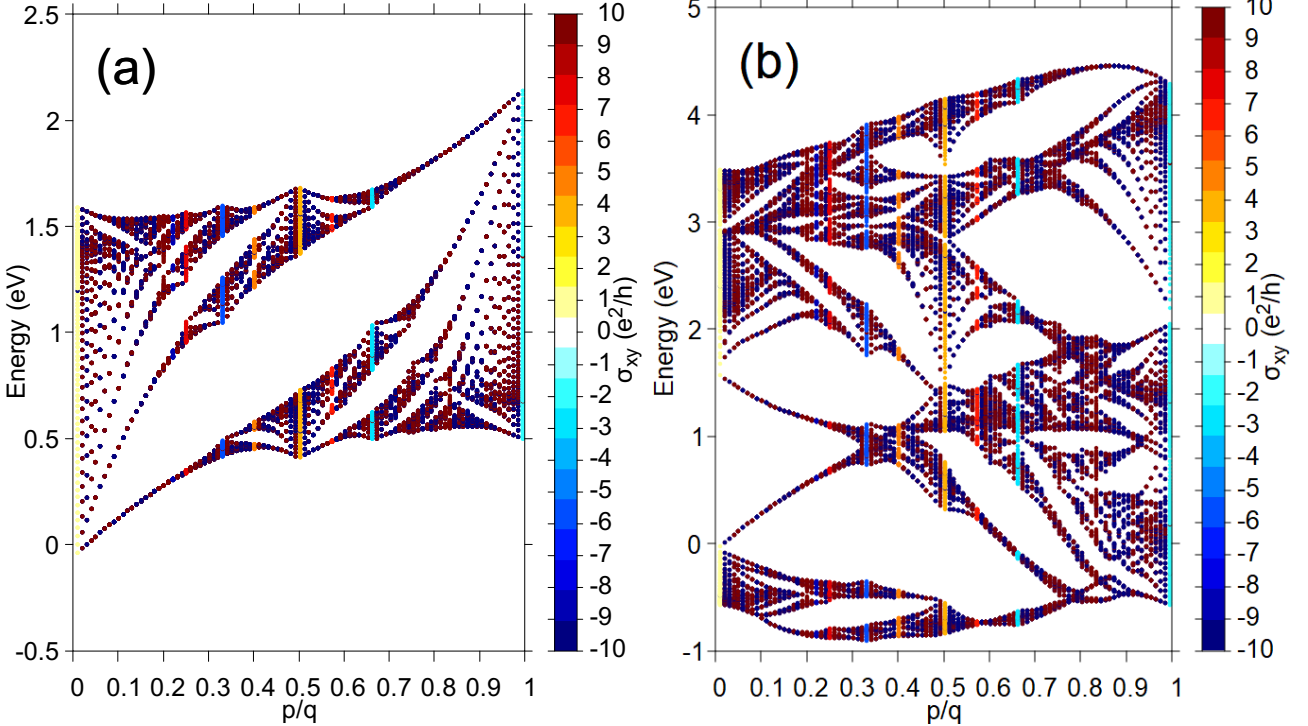


Figure 2.13: Colored points version of Hofstadter butterfly.

Fig 2.14 displays the Hofstadter butterfly, color-coded according to the Hall conductance. Moreover, the number p increases simultaneously with Chern number, making it challenging to maintain a fixed scale. Addressing this, we limit the Chern number scale within $-10 \leq \nu \leq 10$, any Chern number outside this range is set to zero. Regions with zero Hall conductance and the corresponding spectrum are left blank. Remarkably, the two largest gaps near the center of the figure are associated with small integers where the color coding accurately reflects their values. Unlike the traditional Hofstadter butterfly, which highlights the spectrum, this version emphasizes the gaps by using a color scheme to characterize different Hall conductance.

Both figures display rich physics insights, it totally use two different methods to color the butterfly. While Figure 2.14 assigns colors based on the sum of the Chern numbers of the occupied bands, Figure 2.14 colors the gap according to the Chern number that corresponded to each gap index. However, the colored spectrum do more than highlighting the topological properties of the system, they both also explain the behaviour of electrons in a symmetry lattice. Such as, doping a fixed number of electrons will cause a Fermi level change, which is reflected in changes to the Density of state (DOS), captured in Figure (2.14). In addition as the magnetic field increases, there are

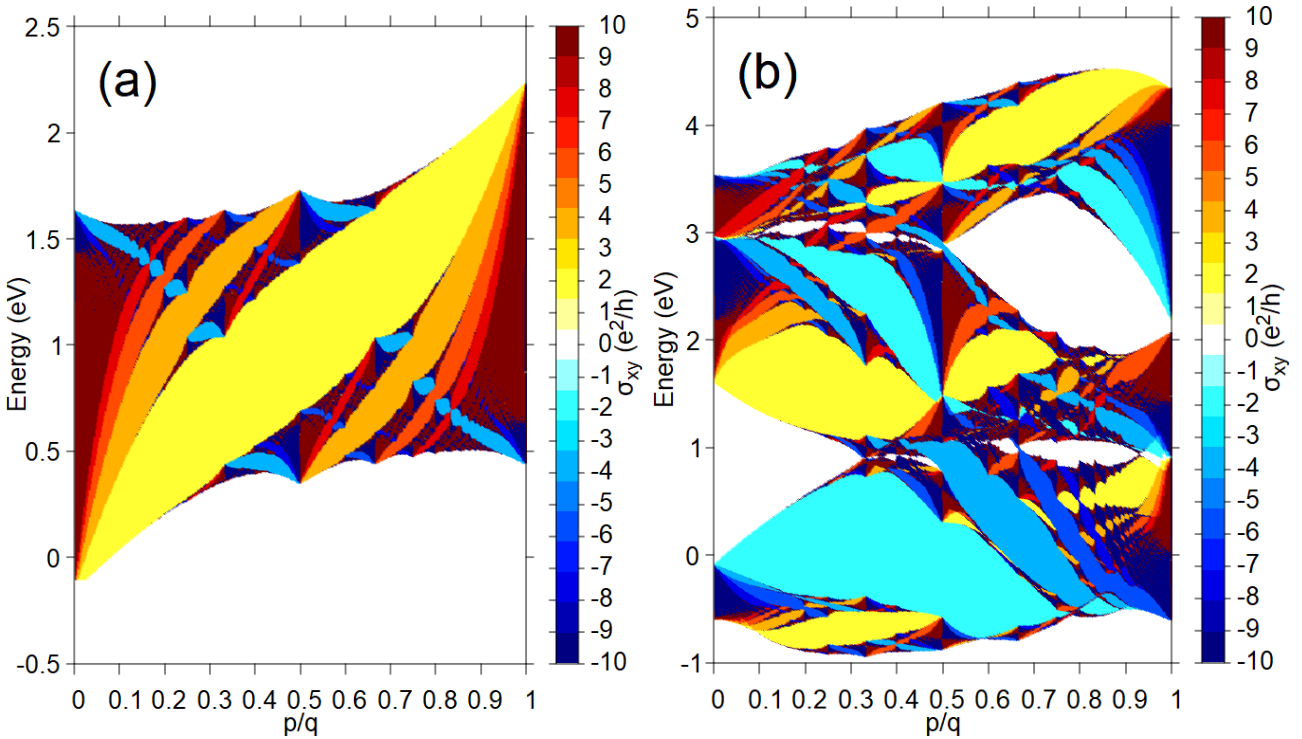


Figure 2.14: Gaps color-coded Hofstadter butterfly. This idea was first made by Avron *et al*[1].

fewer bands occupied. One might ask where the electrons goes. They still there, but not in the bands.

Conclusion, the Hofstadter butterfly provides deep insights into both the quantum Hall effect and the topological properties of monolayer TMD. As we look ahead, studying the Hofstadter physics in novel material systems play an important role in giving opportunities in understanding condensed matter physics.

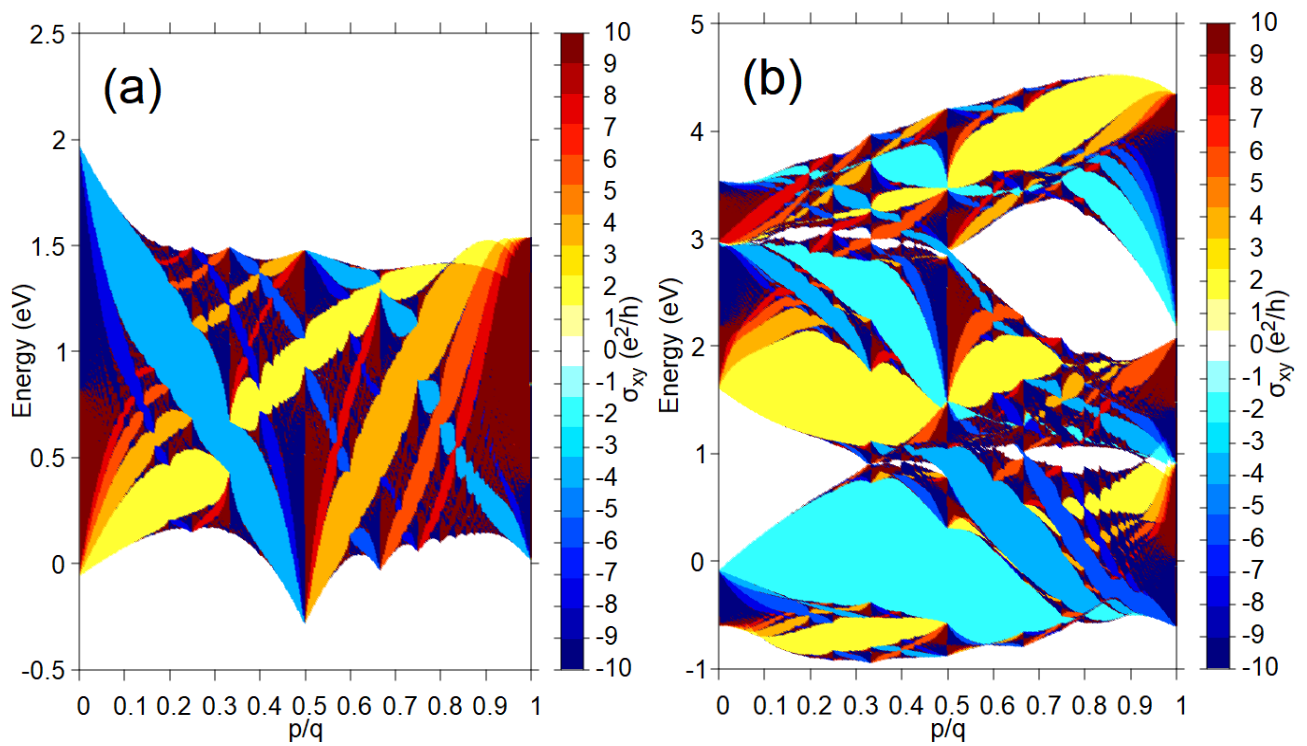


Figure 2.15: Gaps color-coded Hofstadter butterfly. This idea was first made by Avron *et al*[1].

CHAPTER 3

SUMMARY

3.1 Conclusions

In our research, we have calculated the Hofstadter butterfly of monolayer MoS₂ and others transition metal dichalcogenide types by using a tight-binding three-band model. In addition, we have explored the rich and complex physics of monolayer MoS₂, such as Landau levels and integer quantum Hall effect (IQHE), in the presence of external magnetic fields. The research conducted within these pages has demonstrated the unique interplay between the superlattice and magnetic fields, which leads to the emergence of fascinating quantum phenomena.

In section 2.1, we have studied the tight-binding three-band model for monolayers of MX₂ using only the M- d_{z^2} , d_{xy} and $d_{x^2-y^2}$ orbitals. When only NN M-M hoppings are included, we calculated the hopping energies using the symmetry of the D_{3h} point group we derived nineteen hopping parameters from Ref [2].

In section 2.2, we focused on the Hofstadter physics in monolayer TMD, where the lattice gives rise to a rich Hofstadter spectrum when subjected to a magnetic field. The detailed analysis revealed key features of the spectrum, including the SOC and the emergence of topological quantum Hall states.

In section 2.3 and section 2.4, extended the investigation into the realm of Hall effects, introducing the Landau levels, the integer quantum Hall effect and applying it to monolayer TMD systems. We also shown that how the Hofstadter butterfly can be colored in various ways by using the Chern number.

Overall, while this study provides valuable insights, we acknowledge several limitations. Firstly, in section 2.3, our calculation was restricted to the single-band approximation due to the computational complexity of multi-band interactions. Specifically, incorporating three-band model would require significantly more resources, particularly

in calculating Chern numbers, which are numerically intensive for larger Hamiltonian matrices, this significantly cause a time consumption. For example, to achived the colored butterfly, it costs us around two days for a better resolution.

3.2 Discussions and Future work

In this work, we have calculated the Hofstadter butterfly of monolayer MX_2 using a TB three-band model. Group theory was used to defined the hopping parameters. On the one hand, the NN by Liu *et al.* gives rise to a well-fitted highest valence band (VB). However, except for the states nearby the K point, it does not produce an expected band stucture for the other energy bands, even for the lowest conduction band (CB). In contrast, the TNN model with nineteen parameters achieves much better overall fit to the DFT results for all three energy bands, including two CBs and one VB. It hints that the NN and TNN M–M hoppings play an important role. On the other hand, since only d orbitals of M atoms were taken into account in a construction of these two model, they are not applicable to the systems with defect, which often introduced by chalcogen atoms in the lattice. For other simple applications theoretical framework, we can intergrate with the NN model, but in some more complex model it is crucial to consider the TNN the implications of these findings in the context.

APPENDIX A

Matrix elements of the TB Hamiltonian without SOC

In this appendix, we show the matrix elements of the TB Hamiltonian in the absence of SOC that are listed below.

$$\begin{aligned} \mathcal{E}(\mathbf{R}_2) &= D(\sigma'_\nu) \mathcal{E}(\mathbf{R}_1) D^\dagger(\sigma'_\nu) \\ &= \begin{pmatrix} t_0 & \frac{1}{2}t_1 - \frac{\sqrt{3}}{2}t_2 & -\frac{\sqrt{3}}{2}t_1 - \frac{1}{2}t_2 \\ -\frac{1}{2}t_1 - \frac{\sqrt{3}}{2}t_2 & \frac{1}{4}t_{11} + \frac{3}{4}t_{22} & -\frac{\sqrt{3}}{4}t_{11} - t_{12} + \frac{\sqrt{3}}{4}t_{22} \\ \frac{\sqrt{3}}{2}t_1 - \frac{1}{2}t_2 & -\frac{\sqrt{3}}{4}t_{11} + t_{12} + \frac{\sqrt{3}}{4}t_{22} & \frac{3}{4}t_{11} + \frac{1}{4}t_{22} \end{pmatrix}, \end{aligned} \quad (\text{A.1})$$

$$\begin{aligned} \mathcal{E}(\mathbf{R}_3) &= D(C(-\frac{2\pi}{3})) \mathcal{E}(\mathbf{R}_1) D^\dagger(C(-\frac{2\pi}{3})) \\ &= \begin{pmatrix} t_0 & -\frac{1}{2}t_1 + \frac{\sqrt{3}}{2}t_2 & -\frac{\sqrt{3}}{2}t_1 - \frac{1}{2}t_2 \\ \frac{1}{2}t_1 + \frac{\sqrt{3}}{2}t_2 & \frac{1}{4}t_{11} + \frac{3}{4}t_{22} & \frac{\sqrt{3}}{4}t_{11} + t_{12} - \frac{\sqrt{3}}{4}t_{22} \\ \frac{\sqrt{3}}{2}t_1 - \frac{1}{2}t_2 & \frac{\sqrt{3}}{4}t_{11} - t_{12} - \frac{\sqrt{3}}{4}t_{22} & \frac{3}{4}t_{11} + \frac{1}{4}t_{22} \end{pmatrix}, \end{aligned} \quad (\text{A.2})$$

$$\mathcal{E}(\mathbf{R}_4) = D(\sigma_\nu) \mathcal{E}(\mathbf{R}_1) D^\dagger(\sigma_\nu) = \begin{pmatrix} t_0 & -t_1 & t_2 \\ t_1 & t_{11} & -t_{12} \\ t_2 & t_{12} & t_{22} \end{pmatrix}, \quad (\text{A.3})$$

$$\begin{aligned} \mathcal{E}(\mathbf{R}_5) &= D(C(-\frac{4\pi}{3})) \mathcal{E}(\mathbf{R}_1) D^\dagger(C(-\frac{4\pi}{3})) \\ &= \begin{pmatrix} t_0 & -\frac{1}{2}t_1 - \frac{\sqrt{3}}{2}t_2 & \frac{\sqrt{3}}{2}t_1 - \frac{1}{2}t_2 \\ \frac{1}{2}t_1 - \frac{\sqrt{3}}{2}t_2 & \frac{1}{4}t_{11} + \frac{3}{4}t_{22} & -\frac{\sqrt{3}}{4}t_{11} + t_{12} + \frac{\sqrt{3}}{4}t_{22} \\ -\frac{\sqrt{3}}{2}t_1 - \frac{1}{2}t_2 & -\frac{\sqrt{3}}{4}t_{11} - t_{12} + \frac{\sqrt{3}}{4}t_{22} & \frac{3}{4}t_{11} + \frac{1}{4}t_{22} \end{pmatrix}, \end{aligned} \quad (\text{A.4})$$

$$\begin{aligned} \mathcal{E}(\mathbf{R}_6) &= D(\sigma''_\nu) \mathcal{E}(\mathbf{R}_1) D^\dagger(\sigma''_\nu) \\ &= \begin{pmatrix} t_0 & \frac{1}{2}t_1 + \frac{\sqrt{3}}{2}t_2 & \frac{\sqrt{3}}{2}t_1 - \frac{1}{2}t_2 \\ -\frac{1}{2}t_1 + \frac{\sqrt{3}}{2}t_2 & \frac{1}{4}t_{11} + \frac{3}{4}t_{22} & \frac{\sqrt{3}}{4}t_{11} - t_{12} - \frac{\sqrt{3}}{4}t_{22} \\ -\frac{\sqrt{3}}{2}t_1 - \frac{1}{2}t_2 & \frac{\sqrt{3}}{4}t_{11} - t_{12} - \frac{\sqrt{3}}{4}t_{22} & \frac{3}{4}t_{11} + \frac{1}{4}t_{22} \end{pmatrix}, \end{aligned} \quad (\text{A.5})$$

$$\begin{aligned}
\mathcal{E}(\tilde{\mathbf{R}}_2) &= D(C(-\frac{4\pi}{3}))\mathcal{E}(\tilde{\mathbf{R}}_4)D^\dagger(C(-\frac{4\pi}{3})) \\
&= \begin{pmatrix} r_0 & 0 & \frac{2r_2}{\sqrt{3}} \\ 0 & r_{11} + \sqrt{3}r_{12} & 0 \\ \frac{2r_1}{\sqrt{3}} & 0 & r_{11} - \frac{r_{12}}{\sqrt{3}} \end{pmatrix} \tag{A.6}
\end{aligned}$$

$$\begin{aligned}
\mathcal{E}(\tilde{\mathbf{R}}_3) &= D(\sigma_\nu)\mathcal{E}(\tilde{\mathbf{R}}_1)D^\dagger(\sigma_\nu) \\
&= \begin{pmatrix} r_0 & -r_1 & -\frac{r_1}{\sqrt{3}} \\ -r_2 & r_{11} & -r_{12} \\ -\frac{r_2}{\sqrt{3}} & -r_{12} & r_{11} + \frac{2r_{12}}{\sqrt{3}} \end{pmatrix} \tag{A.7}
\end{aligned}$$

$$\begin{aligned}
\mathcal{E}(\tilde{\mathbf{R}}_5) &= D(C(-\frac{4\pi}{3}))\mathcal{E}(\tilde{\mathbf{R}}_1)D^\dagger(C(-\frac{4\pi}{3})) \\
&= \begin{pmatrix} r_0 & 0 & \frac{2r_1}{\sqrt{3}} \\ 0 & r_{11} + \sqrt{3}r_{12} & 0 \\ \frac{2r_2}{\sqrt{3}} & 0 & r_{11} - \frac{r_{12}}{\sqrt{3}} \end{pmatrix} \tag{A.8}
\end{aligned}$$

$$\begin{aligned}
\mathcal{E}(\tilde{\mathbf{R}}_6) &= D(\sigma_\nu)\mathcal{E}(\tilde{\mathbf{R}}_4)D^\dagger(\sigma_\nu) \\
&= \begin{pmatrix} r_0 & -r_2 & -\frac{r_2}{\sqrt{3}} \\ -r_1 & r_{11} & -r_{12} \\ -\frac{r_1}{\sqrt{3}} & -r_{12} & r_{11} + \frac{2r_{12}}{\sqrt{3}} \end{pmatrix} \tag{A.9}
\end{aligned}$$

$$\begin{aligned}
\mathcal{E}(\mathbf{R}'_2) &= D(\sigma'_\nu)\mathcal{E}(\mathbf{R}'_1)D^\dagger(\sigma'_\nu) \\
&= \begin{pmatrix} u_0 & \frac{1}{2}u_1 - \frac{\sqrt{3}}{2}u_2 & -\frac{\sqrt{3}}{2}u_1 - \frac{1}{2}u_2 \\ -\frac{1}{2}u_1 - \frac{\sqrt{3}}{2}u_2 & \frac{1}{4}u_{11} + \frac{3}{4}u_{22} & -\frac{\sqrt{3}}{4}u_{11} - u_{12} + \frac{\sqrt{3}}{4}u_{22} \\ \frac{\sqrt{3}}{2}u_1 - \frac{1}{2}u_2 & -\frac{\sqrt{3}}{4}u_{11} + u_{12} + \frac{\sqrt{3}}{4}u_{22} & \frac{3}{4}u_{11} + \frac{1}{4}u_{22} \end{pmatrix}, \tag{A.10}
\end{aligned}$$

$$\begin{aligned}
\mathcal{E}(\mathbf{R}'_3) &= D(C(-\frac{2\pi}{3}))\mathcal{E}(\mathbf{R}'_1)D^\dagger(C(-\frac{2\pi}{3})) \\
&= \begin{pmatrix} u_0 & -\frac{1}{2}u_1 + \frac{\sqrt{3}}{2}u_2 & -\frac{\sqrt{3}}{2}u_1 - \frac{1}{2}u_2 \\ \frac{1}{2}u_1 + \frac{\sqrt{3}}{2}u_2 & \frac{1}{4}u_{11} + \frac{3}{4}u_{22} & \frac{\sqrt{3}}{4}u_{11} + u_{12} - \frac{\sqrt{3}}{4}u_{22} \\ \frac{\sqrt{3}}{2}u_1 - \frac{1}{2}u_2 & \frac{\sqrt{3}}{4}u_{11} - u_{12} - \frac{\sqrt{3}}{4}u_{22} & \frac{3}{4}u_{11} + \frac{1}{4}u_{22} \end{pmatrix}, \tag{A.11}
\end{aligned}$$

$$\mathcal{E}(\mathbf{R}'_4) = D(\sigma_\nu)\mathcal{E}(\mathbf{R}'_1)D^\dagger(\sigma_\nu) = \begin{pmatrix} u_0 & -u_1 & u_2 \\ u_1 & u_{11} & -u_{12} \\ u_2 & u_{12} & u_{22} \end{pmatrix}, \tag{A.12}$$

$$\begin{aligned}
\mathcal{E}(\mathbf{R}'_5) &= D(C(-\frac{4\pi}{3}))\mathcal{E}(\mathbf{R}'_1)D^\dagger(C(-\frac{4\pi}{3})) \\
&= \begin{pmatrix} u_0 & -\frac{1}{2}u_1 - \frac{\sqrt{3}}{2}u_2 & \frac{\sqrt{3}}{2}u_1 - \frac{1}{2}u_2 \\ \frac{1}{2}u_1 - \frac{\sqrt{3}}{2}u_2 & \frac{1}{4}u_{11} + \frac{3}{4}u_{22} & -\frac{\sqrt{3}}{4}u_{11} + u_{12} + \frac{\sqrt{3}}{4}u_{22} \\ -\frac{\sqrt{3}}{2}u_1 - \frac{1}{2}u_2 & -\frac{\sqrt{3}}{4}u_{11} - u_{12} + \frac{\sqrt{3}}{4}u_{22} & \frac{3}{4}u_{11} + \frac{1}{4}u_{22} \end{pmatrix}, \tag{A.13}
\end{aligned}$$

$$\begin{aligned}
\mathcal{E}(\mathbf{R}'_6) &= D(\sigma''_\nu) \mathcal{E}(\mathbf{R}'_1) D^\dagger(\sigma''_\nu) \\
&= \begin{pmatrix} u_0 & \frac{1}{2}u_1 + \frac{\sqrt{3}}{2}u_2 & \frac{\sqrt{3}}{2}u_1 - \frac{1}{2}u_2 \\ -\frac{1}{2}u_1 + \frac{\sqrt{3}}{2}u_2 & \frac{1}{4}u_{11} + \frac{3}{4}u_{22} & \frac{\sqrt{3}}{4}u_{11} - u_{12} - \frac{\sqrt{3}}{4}u_{22} \\ -\frac{\sqrt{3}}{2}u_1 - \frac{1}{2}u_2 & \frac{\sqrt{3}}{4}u_{11} - u_{12} - \frac{\sqrt{3}}{4}u_{22} & \frac{3}{4}u_{11} + \frac{1}{4}u_{22} \end{pmatrix}, \quad (\text{A.14})
\end{aligned}$$

In Eqs (A.1) to (A.14), t, u and r are the hopping parameters and $D(g_n)$ is the matrix of the irreducible representation (see Tables A.1 and A.2).

	$a(\text{\AA})$	ϵ_1	ϵ_2	t_0	t_1	t_2	t_{11}	t_{12}	t_{22}
GGA									
MoS ₂	3.190	1.046	2.104	-0.184	0.401	0.507	0.218	0.338	0.057
WS ₂	3.191	1.130	2.275	-0.206	0.567	0.536	0.286	0.384	-0.061
MoSe ₂	3.326	0.919	2.065	-0.188	0.317	0.456	0.211	0.290	0.130
WSe ₂	3.325	0.943	2.179	-0.207	0.457	0.486	0.263	0.329	0.034
MoTe ₂	3.557	0.605	1.972	-0.169	0.228	0.390	0.207	0.239	0.252
WTe ₂	3.560	0.606	2.102	-0.175	0.342	0.410	0.233	0.270	0.190
LDA									
MoS ₂	3.129	1.238	2.366	-0.218	0.444	0.533	0.250	0.360	0.047
WS ₂	3.132	1.355	2.569	-0.238	0.626	0.557	0.324	0.405	-0.076
MoSe ₂	3.254	1.001	2.239	-0.222	0.350	0.488	0.244	0.314	0.129
WSe ₂	3.253	1.124	2.447	-0.242	0.506	0.514	0.305	0.353	0.025
MoTe ₂	3.472	0.618	2.126	-0.202	0.254	0.423	0.241	0.263	0.269
WTe ₂	3.476	0.623	2.251	-0.209	0.388	0.442	0.272	0.295	0.200

Table A.1: Fitted parameters in three-band NN TBM for both GGA and LDA cases for MX₂ [2].

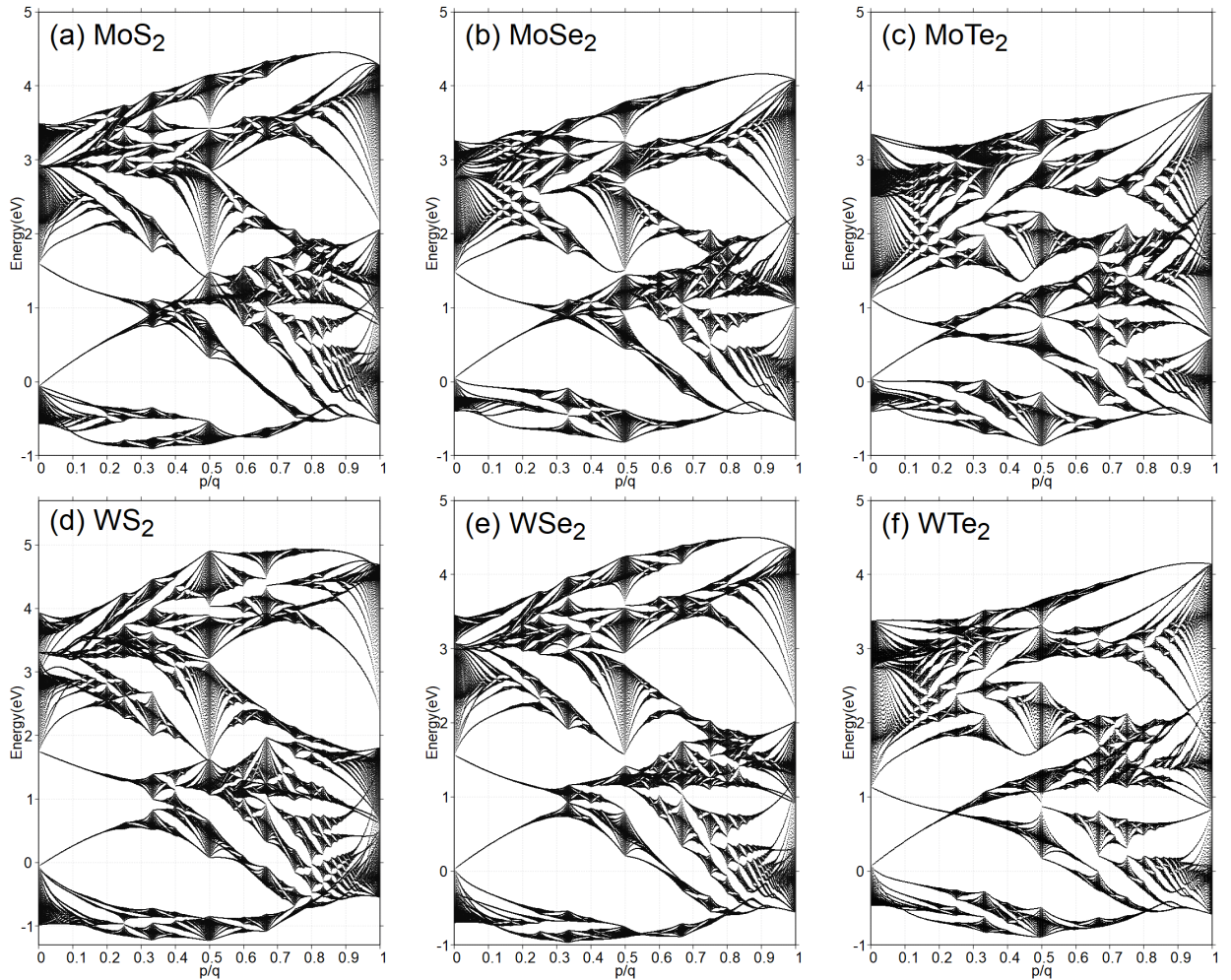


Figure A.1: The NN Hofstadter's butterflies of MX_2 monolayers using GGA parameters from Table A.1.

	$a(\text{\AA})$	ϵ_1	ϵ_2	t_0	t_1	t_2	t_{11}	t_{12}	t_{22}	r_0
	r_1	r_2	r_{11}	r_{12}	u_0	u_1	u_2	u_{11}	u_{12}	u_{22}
GGA										
MoS ₂	3.190	0.683	1.707	-0.146	-0.114	0.506	0.085	0.162	0.073	0.060
	-0.236	0.067	0.016	0.087	-0.038	0.046	0.001	0.266	-0.176	-0.150
WS ₂	3.191	0.717	1.916	-0.152	-0.097	0.590	0.047	0.178	0.016	0.069
	-0.261	0.107	-0.003	0.109	-0.054	0.045	0.002	0.325	-0.206	-0.163
MoSe ₂	3.326	0.684	1.546	-0.146	-0.130	0.432	0.144	0.117	0.075	0.039
	-0.209	0.069	0.052	0.060	-0.042	0.036	0.008	0.272	-0.172	-0.150
WSe ₂	3.325	0.728	1.655	-0.146	-0.124	0.507	0.117	0.127	0.015	0.036
	-0.234	0.107	0.044	0.075	-0.061	0.032	0.007	0.329	-0.202	-0.164
MoTe ₂	3.357	0.588	1.303	-0.226	-0.234	0.036	0.400	0.098	0.017	0.003
	-0.025	-0.169	0.082	0.051	0.057	0.103	0.187	-0.045	-0.141	0.087
WTe ₂	3.560	0.697	1.380	-0.109	-0.164	0.368	0.204	0.093	0.038	-0.015
	-0.209	0.107	0.115	0.009	-0.066	0.011	-0.013	0.312	-0.177	-0.132
LDA										
MoS ₂	3.190	0.820	1.931	-0.176	-0.101	0.531	0.084	0.169	0.070	0.070
	-0.252	0.084	0.019	0.093	-0.043	0.047	0.005	0.304	-0.192	-0.162
WS ₂	3.191	0.905	2.167	-0.175	-0.090	0.611	0.043	0.181	0.008	0.075
	-0.282	0.127	0.001	0.114	-0.063	0.047	0.004	0.374	-0.224	-0.177
MoSe ₂	3.326	0.715	1.687	-0.154	-0.134	0.437	0.124	0.119	0.072	0.048
	-0.248	0.090	0.066	0.045	-0.067	0.041	0.005	0.327	-0.194	-0.151
WSe ₂	3.325	0.860	1.892	-0.152	-0.125	0.508	0.094	0.129	0.009	0.044
	-0.278	0.129	0.059	0.058	-0.090	0.039	0.001	0.392	-0.224	-0.165
MoTe ₂	3.357	0.574	1.410	-0.148	-0.173	0.333	0.203	0.186	0.127	0.007
	-0.280	-0.067	0.073	0.081	-0.054	0.008	0.037	0.145	-0.078	0.035
WTe ₂	3.560	0.675	1.489	-0.124	-0.159	0.362	0.196	0.101	0.044	-0.009
	-0.250	0.129	0.131	-0.007	-0.086	0.012	-0.020	0.361	-0.193	-0.129

Table A.2: Fitted parameters in three-band TNN TBM for both GGA and LDA cases for MX₂ [2].

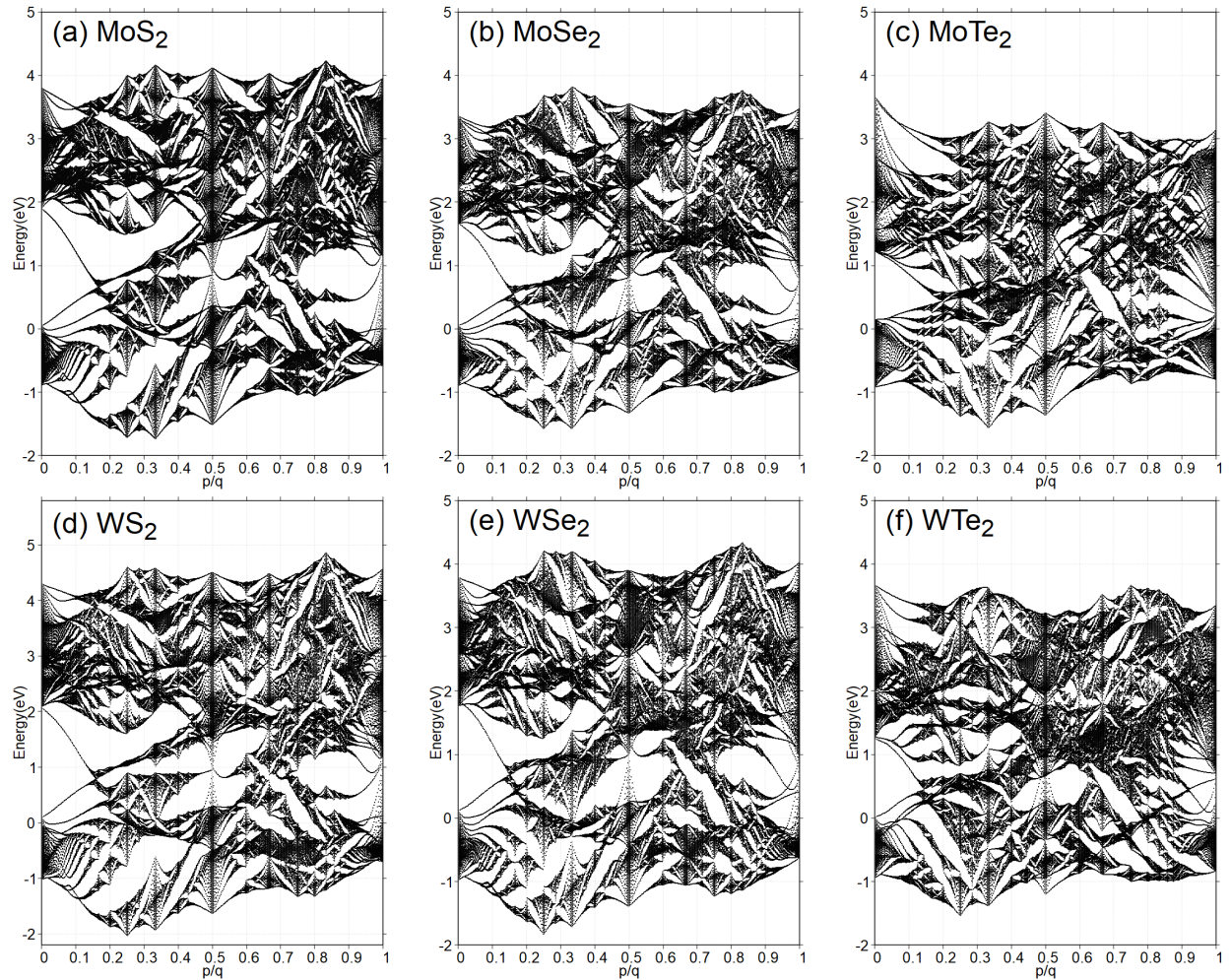


Figure A.2: The TNN Hofstadter's butterflies of MX_2 monolayers using GGA parameters from Table A.2.

APPENDIX B

Details of the Peierls substitution

As we mentioned in Section 2.2, we work in the Landau gauge $\mathbf{A} = (By, 0, 0)$. The Peierls phase is given as $\theta_{i,i'} = \int_i^{i'} \mathbf{A} \cdot d\mathbf{r}$. By making an parametrization, for instance

$$\begin{cases} x = x_m + (x_{m'} - x_m)\tau, \\ y = y_n + (y_{n'} - y_n)\tau, \end{cases} \quad (\text{B.1})$$

where $\tau \in [0, 1]$ and $i = (m, n)$, thanks to the Landau gauge, the path integral resembles to $\int Bx dy$, the phases can be written as

$$\begin{aligned} \theta_{i,i'} &= \frac{eB}{\hbar} \int_0^1 [x_m + (x_{m'} - x_m)\tau] (y_{n'} - y_n) d\tau \\ &= \frac{eB}{\hbar} \left(x_m + \frac{x_{m'} - x_m}{2} \right) (y_{n'} - y_n) \\ &= \frac{eB}{\hbar} \left(\frac{x_m + x_{m'}}{2} \right) (y_{n'} - y_n). \end{aligned} \quad (\text{B.2})$$

From this, the Peierls phase depends on absolute x coordinates but only relative to y coordinates.

APPENDIX C

Solving the Diophantine equation

We have defined the magnetic flux through a unit cell is $\frac{\Phi}{\Phi_0} = \frac{p}{q}$. Given p and q are mutually prime numbers, we set the pairs $(\nu_r, s_r) = (m, n)$ as the solution of the Diophantine equation.

$$pm + qn = r. \quad (\text{C.1})$$

By using Euclidean algorithm, we can obtain (m, n) . For instance, taking the rational flux ratio is $p/q = 4/13$, thus the Chern number goes from -6 to 6 , and the equation (C.1) becomes

$$r = 4m + 13n. \quad (\text{C.2})$$

In the meantime, the gap index n now varies from $-q$ to q due to the butterfly's symmetry. Each value of r , going from 0 to $q - 1$ only have one couple of valid (m, n) . The values of r are depicted in Table C.1

r	0	1	2	3	4	5	6	7	8	9	10	11	12
m	0	-3	-6	4	1	-2	-5	5	2	-1	-4	-6	3
n	0	1	2	-1	0	1	2	-1	0	1	2	-1	0

Table C.1: Allowed values of r .

REFERENCES

- [1] Joseph E Avron, Daniel Osadchy, and Ruedi Seiler. A topological look at the quantum hall effect. *Physics today*, 56(8):38–42, 2003.
- [2] Gui-Bin Liu, Wen-Yu Shan, Yugui Yao, Wang Yao, and Di Xiao. Three-band tight-binding model for monolayers of group-vib transition metal dichalcogenides. *Phys. Rev. B*, 88:085433, Aug 2013.
- [3] Fırat Yalçın. Tight binding investigation of graphene nanostructures under magnetic field. Master’s thesis, Middle East Technical University, 2019.
- [4] Douglas R. Hofstadter. Energy levels and wave functions of bloch electrons in rational and irrational magnetic fields. *Phys. Rev. B*, 14:2239–2249, Sep 1976.
- [5] Yakir Aharonov and David Bohm. Significance of electromagnetic potentials in the quantum theory. *Physical review*, 115(3):485–497, 1959.
- [6] R Rammal. Landau level spectrum of bloch electrons in a honeycomb lattice. *Journal de Physique*, 46(8):1345–1354, 1985.
- [7] James G. Analytis, Stephen J. Blundell, and Arzhang Ardavan. Landau levels, molecular orbitals, and the hofstadter butterfly in finite systems. *American Journal of Physics*, 72(5):613–618, 05 2004.
- [8] D. Shoenberg. *Magnetic Oscillations in Metals*. Cambridge Monographs on Physics. Cambridge University Press, 1984.
- [9] J. Singleton. *Band Theory and Electronic Properties of Solids*. Oxford Master Series in Condensed Matter Physics. OUP Oxford, 2001.
- [10] S. Blundell. *Magnetism in Condensed Matter*. Oxford Master Series in Condensed Matter Physics 4. OUP Oxford, 2001.
- [11] C. Kittel. *Quantum Theory of Solids*. Wiley, 1987.
- [12] Juan Li, Yi-Fei Wang, and Chang-De Gong. Tight-binding electrons on triangular and kagomé lattices under staggered modulated magnetic fields: quantum

hall effects and hofstadter butterflies. *Journal of Physics: Condensed Matter*, 23(15):156002, apr 2011.

- [13] K. v. Klitzing, G. Dorda, and M. Pepper. New method for high-accuracy determination of the fine-structure constant based on quantized hall resistance. *Phys. Rev. Lett.*, 45:494–497, Aug 1980.
- [14] Mahito Kohmoto. Zero modes and the quantized hall conductance of the two-dimensional lattice in a magnetic field. *Physical Review B*, 39(16):11943, 1989.
- [15] Yasuhiro Hatsugai and Mahito Kohmoto. Energy spectrum and the quantum hall effect on the square lattice with next-nearest-neighbor hopping. *Physical review B*, 42(13):8282, 1990.
- [16] Mahito Kohmoto. Topological invariant and the quantization of the hall conductance. *Annals of Physics*, 160(2):343–354, 1985.
- [17] D. J. Thouless, M. Kohmoto, M. P. Nightingale, and M. den Nijs. Quantized hall conductance in a two-dimensional periodic potential. *Phys. Rev. Lett.*, 49:405–408, Aug 1982.
- [18] P Streda. Theory of quantised hall conductivity in two dimensions. *Journal of Physics C: Solid State Physics*, 15(22):L717, 1982.
- [19] Francesco Di Colandrea, Alessio d’Errico, Maria Maffei, Hannah M Price, Maciej Lewenstein, Lorenzo Marrucci, Filippo Cardano, Alexandre Dauphin, and Pietro Massignan. Linking topological features of the hofstadter model to optical diffraction figures. *New Journal of Physics*, 24(1):013028, 2022.
- [20] Itzhack Dana, Yosi Avron, and J Zak. Quantised hall conductance in a perfect crystal. *Journal of Physics C: Solid State Physics*, 18(22):L679, 1985.
- [21] Godfrey Gumbs and Paula Fekete. Hofstadter butterfly for the hexagonal lattice. *Phys. Rev. B*, 56:3787–3791, Aug 1997.
- [22] Philip George Harper. The general motion of conduction electrons in a uniform magnetic field, with application to the diamagnetism of metals. *Proceedings of the Physical Society. Section A*, 68(10):879–892, 1955.
- [23] Andor Kormányos, Viktor Zólyomi, Neil D. Drummond, Péter Rakyta, Guido Burkard, and Vladimir I. Fal’ko. Monolayer mos₂: Trigonal warping, the Γ valley, and spin-orbit coupling effects. *Phys. Rev. B*, 88:045416, Jul 2013.
- [24] Branimir Radisavljevic, Aleksandra Radenovic, Jacopo Brivio, Valentina Gi-

cometti, and Andras Kis. Single-layer mos2 transistors. *Nature nanotechnology*, 6(3):147–150, 2011.

- [25] Fengyuan Xuan and Su Ying Quek. Valley zeeman effect and landau levels in two-dimensional transition metal dichalcogenides. *Phys. Rev. Res.*, 2:033256, Aug 2020.
- [26] Jun John Sakurai and Jim Napolitano. *Modern quantum mechanics*. Cambridge University Press, 2020.
- [27] Rudolph Peierls. Zur theorie des diamagnetismus von leitungselektronen. *Zeitschrift für Physik*, 80(11):763–791, 1933.
- [28] Gi-Yeong Oh. Energy spectrum of a triangular lattice in a uniform magnetic field: Effect of next-nearest-neighbor hopping. *Journal of the Korean Physical Society*, 37(5):534–539, 2000.
- [29] Jenö Sólyom. *Fundamentals of the Physics of Solids: Volume II: Electronic Properties*, volume 2. Springer Science & Business Media, 2008.
- [30] David J Griffiths and Darrell F Schroeter. *Introduction to quantum mechanics*. Cambridge university press, 2018.
- [31] GH Wannier. A result not dependent on rationality for bloch electrons in a magnetic field. *physica status solidi (b)*, 88(2):757–765, 1978.
- [32] Di Xiao, Ming-Che Chang, and Qian Niu. Berry phase effects on electronic properties. *Reviews of modern physics*, 82(3):1959–2007, 2010.